

Viewpoint

Synaptic Odyssey

Kristen M. Harris

Department of Neuroscience, Center for Learning and Memory, University of Texas at Austin, Austin, Texas 78712

Synaptic communication is at the heart of nervous system function. Our understanding of synaptic structure and plasticity has grown enormously since the founding of the Society for Neuroscience 50 years ago. Much insight has come from examining these structures with light and electron microscopy. This photo essay describes my odyssey through the world of synapses. Because the *Journal of Neuroscience* (JN) has accompanied me on this synaptic odyssey, I have organized the figures to feature JN articles that launched each part of the journey. Although the overall story is told in an approximately chronological order, the panels of each figure are topical and spur side trips that are temporally out of sequence. Given the cursory nature of this essay, I encourage you to read the original articles for analytical details and for references to the vast body of literature that supports or contradicts the conclusions reached along the way.

This story began in 1978 with love at first sight, when I first saw dendritic spines studding the surface of Golgi-impregnated neurons in the light microscope (Fig. 1; Harris et al., 1980). I wondered why neurons position excitatory synapses upon the heads of these tiny compartments that separate them from the parent dendrite. In the beginning, I studied dendritic spines with light microscopy, and then with freeze-fracture, which revealed spine profiles and bumps or pits where proteins were in the membranes at the synapse and elsewhere (Fig. 2A; Harris and Landis, 1986). I soon realized, however, that these approaches left too many secrets buried inside the spines and deep in the complex neuropil surrounding them. So, I plunged into three-dimensional reconstruction from serial section electron microscopy (3DEM) to obtain spine dimensions that are still used in modeling structure–function relationships (Fig. 2B; Harris and Stevens, 1989). The results eventually led to the first dense reconstructions in brain tissue and showed that only 20% of axons touching a dendrite actually synapse with that dendrite (Fig. 2C; Mishchenko et al., 2010). The dense reconstructions revealed ~500 synapses in a neuropil volume equal to that of a single red blood cell (Fig. 2D–F; Harris et al., 2015). We learned that the extracellular space is not uniformly distributed but instead forms sheets and tunnels where molecules and other extracellular components could take diverse routes to share information (Fig. 2G; Kinney et al., 2013). Eventually, the original images, tutorials, and reconstructions were made public to the neural circuit and cell biology communities (available at 3DEM.org; Harris et al., 2015).

Received April 1, 2019; revised Dec. 1, 2019; accepted Dec. 2, 2019.

The author declares no competing financial interests.

Correspondence should be addressed to Kristen M. Harris at kmh2249@gmail.com.

<https://doi.org/10.1523/JNEUROSCI.0735-19.2019>

Copyright © 2020 the authors

The knowledge gained emphasized the need to go beyond counts and shapes to deduce whether alterations in dendritic spines were the cause or consequence of neural dysfunction (Fig. 2H–K). A thorough review of the literature and our own data suggested that dendritic spines are responsive to upstream degeneration of axons or perisynaptic astroglia, and, instead of causing the illness, their aberrant structures reflect an effort to maintain function as best as possible (Fiala et al., 2002; Witcher et al., 2010; Kuwajima et al., 2013c).

We faced many challenges to ensure that our quantitative analyses provided systematic and unbiased outcomes. The most difficult step was to establish uniform section thickness (Fig. 3A; Harris et al., 2006). We developed a free, quantitative, and easy-to-use reconstruction system (Fig. 3B; Fiala and Harris, 2001a, 2002) and used it to standardize a cylindrical diameters method to ascertain section thickness (Fig. 3C,D; Fiala and Harris, 2001b). The next challenge was to understand the denominator of normalized data (i.e., per area, per volume, per unit length). Initially, we subtracted obliquely sectioned large objects that include cytoplasmic areas where synapses cannot form and are nonuniformly distributed throughout the neuropil (Fig. 3E,F; Harris et al., 1989; 1992). We formalized analyses of unbiased bricks (Fig. 3G) and segment lengths (Fig. 3H; Fiala and Harris, 2001). Another important challenge has been to image large fields with sufficiently high resolution to discern synapses and subcellular components, which was achieved by operating the scanning electron microscope in the transmission mode (tSEM; Kuwajima et al., 2013a,b). With tSEM, whole dendritic arbors (Fig. 3I) can be imaged across just a few montaged fields (Fig. 3J). Traditionally, the high resolution needed to quantify subcellular components required imaging small fields on the transmission electron microscope (TEM). We showed that enough resolution was maintained to distinguish and quantify dimensions and the extent of key subcellular constituents, using the tSEM strategy (Fig. 3K). These approaches made feasible experiments using 3DEM to go beyond the initial, essential descriptions to quantitative outcomes of synaptic dimensions and composition.

We obtained expertise in hippocampal brain slice physiology to investigate structural synaptic plasticity under controlled experimental conditions (Harris and Teyler 1983, 1984; Teyler et al., 1989). We established new methods that produce high-quality tissue preservation in the slices by microwave-enhanced fixation under lukewarm conditions that facilitate diffusion without destroying delicate ultrastructure (Jensen and Harris, 1989). Nevertheless, we faced the well known challenge of slicing-induced alterations in neuronal structure (Fig. 4A,B; Kirov et al., 1999). We discovered that slicing induces synaptogenesis that could not be blocked with

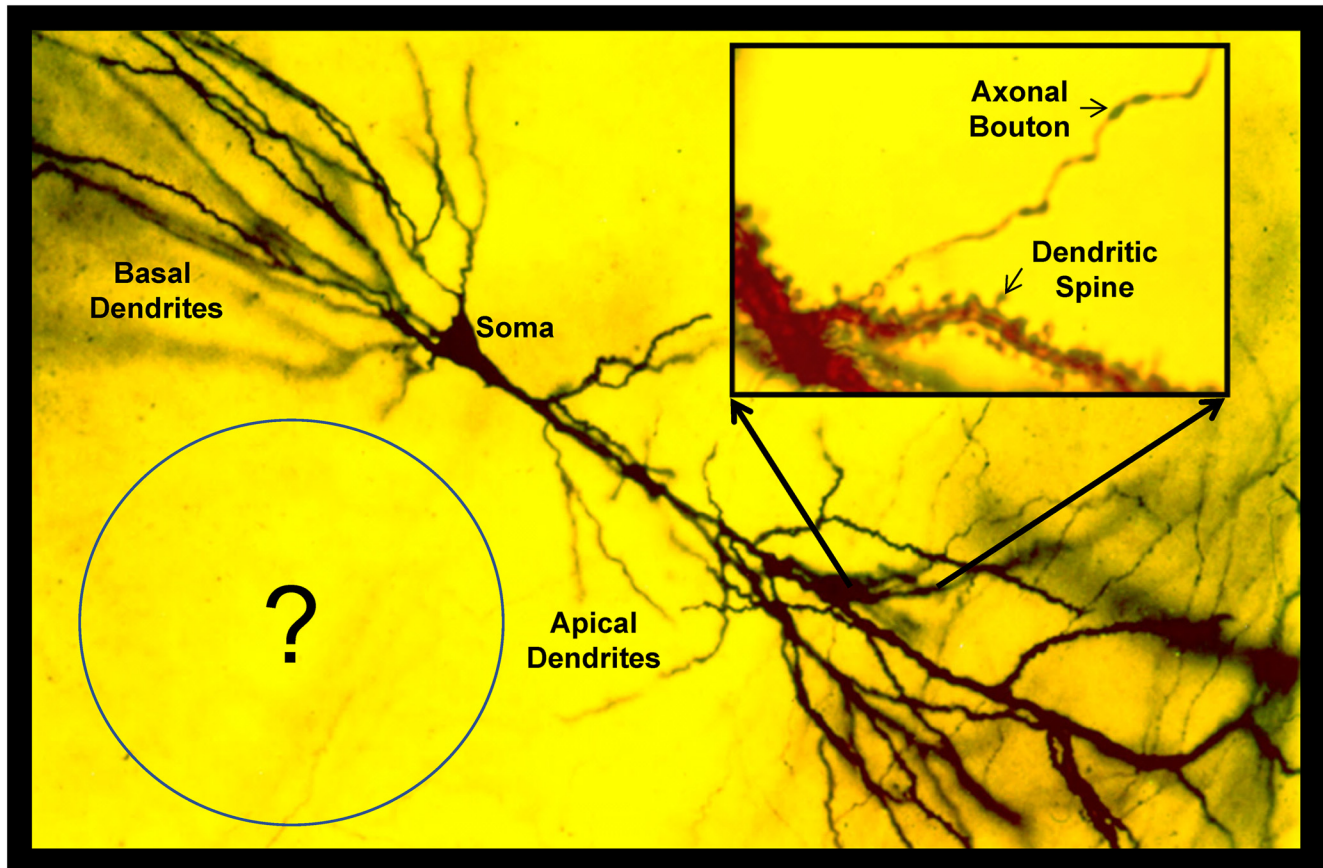


Figure 1. Rapid Golgi preparation from area CA1 in adult rat hippocampus. This technique allows one to see single CA1 pyramidal cells with basal and apical dendrites. With higher magnification (inset), one can see dendritic spines and axonal boutons. But these images raised a question: what is not being visualized in the surrounding neuropil? Adapted from Harris et al., 1980.

activity blockers or with control or tetanic stimulation (Fig. 4C; Kirov and Harris, 1999). Instead the effect was brought on by chilling the slices during preparation (Fig. 4D–H; Kirov et al., 2004). Even with optimal temperature during preparation, 3 h were required for the slices to recover and stabilize (Fig. 4I–Q; Fiala et al., 2003; Bourne et al., 2007).

These experiments prepared us to investigate structural synaptic plasticity following induction of long-term potentiation (LTP), a cellular mechanism of learning. We used a within-slice paradigm to induce LTP at one electrode and showed independence of activation from stimulation at a second electrode located >400 μ m away in the same slice (Fig. 5A, B; Sorra and Harris, 1998; Bourne and Harris, 2011). A similar induction paradigm showed that the distribution of phosphorylated calcium/calmodulin-dependent protein kinase II (P-CaMKII) was restricted to the region beneath the stimulating electrode used for LTP induction and did not spread to the control stimulation site (Fig. 5C; Ouyang et al., 1997). The outcomes of our first study showed stability in average synapse density and size after the induction of LTP with three bouts of tetanic stimulation (1 s at 100 Hz; Fig. 5D–F; Sorra and Harris, 1998).

Adjusting the LTP induction protocol to a more realistic activation pattern known as theta-burst stimulation (TBS; Fig. 5G), revealed a remarkable underlying process. Unlike tetanic stimulation, synapses were enlarged by 2 h after the induction of LTP with TBS (Fig. 5H; Bourne and Harris, 2011). The TBS stalled spine outgrowth, which is normally facilitated by control test-pulse stimulation during slice recovery (Fig. 5I; Bell et al., 2014). The combination of LTP-related synapse enlargement and stalled

spine outgrowth resulted in a constant total synaptic input per unit length of dendrite (Fig. 5J). This homeostatic balance between synapse number and size is characteristic of oblique dendrites in hippocampal area CA1 from young adult rats (60–70 d old; Fig. 5K).

Neurons are not born with dendritic spines. Initially, smooth or varicose dendrites extend filopodia that sometimes form synapses or adhesion junctions and ultimately transport the axons to dendritic shafts (Fig. 6A; Fiala et al., 1998). In the developing hippocampus, the full variety of dendritic spine shapes seen in adults can be observed by postnatal day 15 (P15; Fig. 6B; Harris et al., 1992). Dendritic spines first appear at P11–P12; spine density reaches 50% at P15, and 1 week later reaches 82% of adult levels (Fig. 6C; Kirov et al., 2004). These observations support the hypothesis that normal synaptogenesis proceeds from filopodial contact and axonal migration to the dendrite shaft followed by spine outgrowth (Fig. 6D; Harris, 1999).

We have long wondered whether the effects of functional synaptic plasticity on synapse structure and composition change over the course of maturation. Initially, we found that the earliest age at which we could induce LTP with tetanic stimulation was postnatal day 15 in rat hippocampal area CA1 (Harris and Teyler, 1984; Jackson et al., 1993). In contrast, the earliest age that LTP could be induced by the more robust TBS paradigm coincided with the appearance of dendritic spines at P12 (Fig. 6E; Cao and Harris, 2012). However, applying multiple TBS episodes separated in time by ≥ 90 min can push the onset to a couple of days earlier (Fig. 6F; Cao and Harris, 2012). Notably, when TBS is given at P15, synapses do not enlarge; instead, new

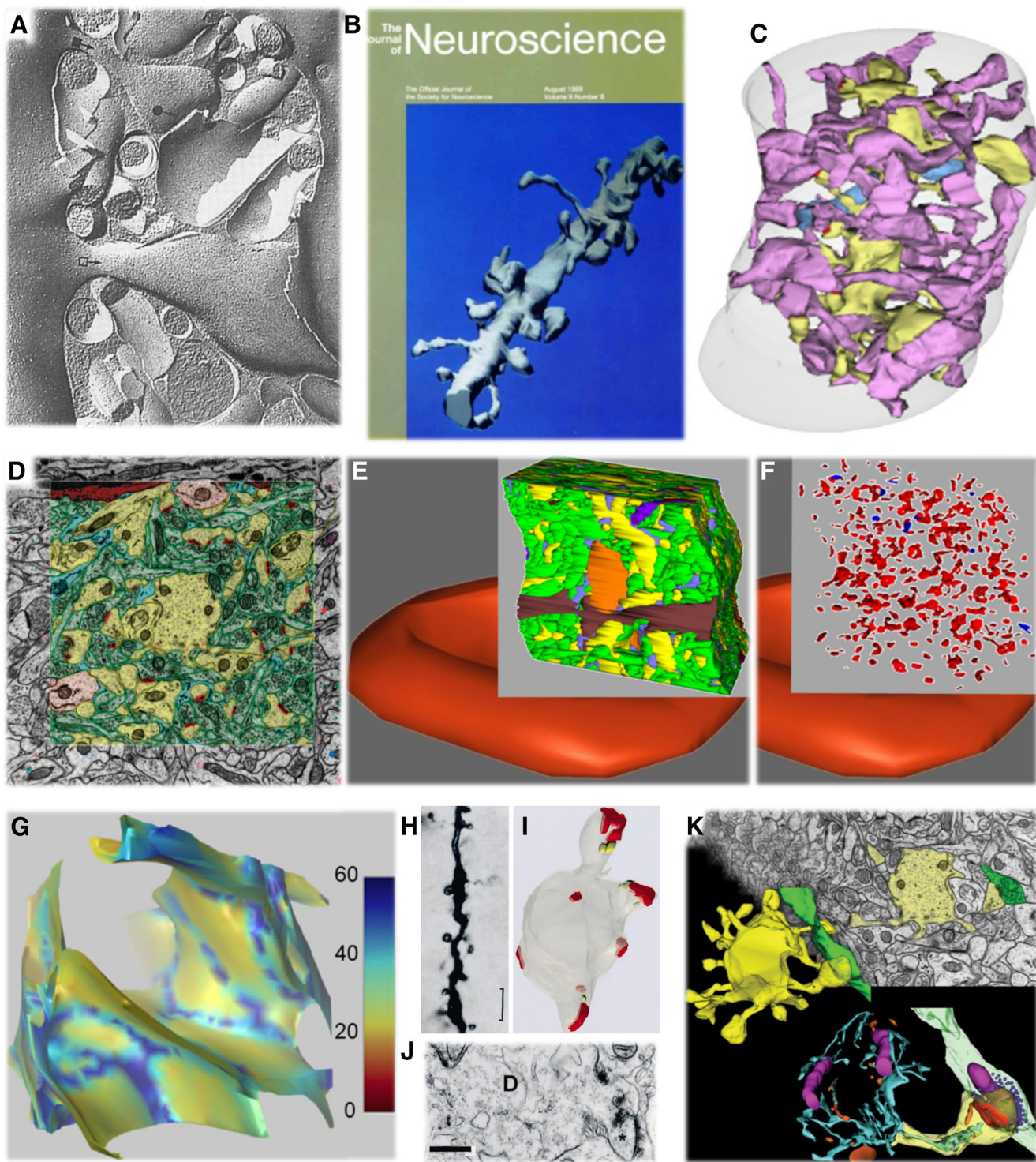


Figure 2. From single dendritic spines to dense reconstructions. **A**, Freeze–fracture image of a small dendritic spine (black filled circles) and a large dendritic spine (open square) seen in profile. Adapted from Lisman and Harris, 1993; original figure is from Harris and Landis, 1986. **B**, First fully surfaced 3D reconstruction from serial electron microscopy sections through a dendritic segment in rat hippocampal area CA1 gracing the cover of *JN* accompanying the article by Harris and Stevens (1989). **C**, Later, additional series were cut from the same rat as in **B**, and dense reconstructions of all elements in the tissue revealed that only 20% of the axons (pink) that touch a dendrite (yellow) actually form a synapse (blue; Mishchenko et al., 2010). **D**, Different dense reconstruction from the same rat hippocampus as in **C** (yellow, spiny dendrites; pale orange, nonspiny dendrites; green, axons; red, synapses; dark orange, microglia; light blue, astroglia). **E**, Tissue section reconstructed in **D** overlaid on a single reconstructed single red blood cell ($\sim 180 \mu\text{m}^3$) to illustrate relative volume. **F**, Removing all elements except synapses shows that the volume reconstructed in **E** contained a total of 498 synapses (red, excitatory; blue, inhibitory). Three of the dense reconstructions from this brain were shared publicly (**D–F** were adapted from Harris et al., 2015). **G**, Extracellular space reconstruction from $1 \mu\text{m}^3$ of the neuropil from **D**. Color code shows sheets at 0–30 nm separation between objects (red–yellow) and larger tunnels at 30–60 nm wide (light to dark blue). Adapted from Kinney et al. (2013). **H–J**, Dendritic spine pathology in human epileptiform cortex: is it a cause or consequence of neuropathology? **H**, Golgi impregnation. Scale bar, 2 μm . **I, J**, 3D and EM. Scale bar, 500 nm. Adapted from Fiala et al. (2002b). **K**, Going beyond counts and shapes helps to determine how the composition of dendritic spines and the surrounding neuropil affects synapses (this picture is from normal rat hippocampus; yellow, dendrite; green, axon; blue and green, SER; purple, mitochondria; orange, endosomes; red, synapse; dark blue, spheres in presynaptic bouton are vesicles. Adapted from the cover of the issue with the article by Kuwajima et al. (2013b).

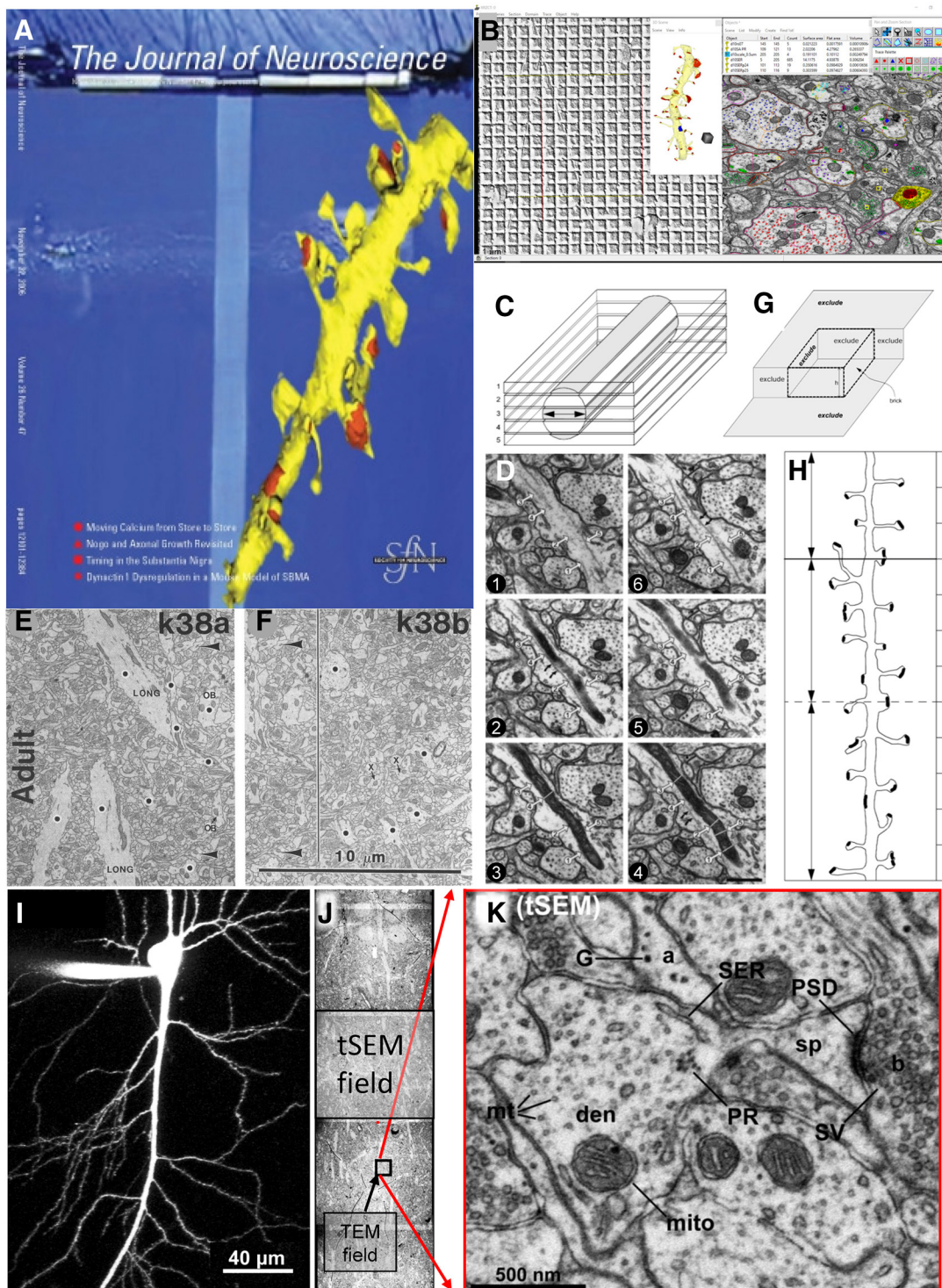


Figure 3. Interpreting quantitative outcomes from serial thin sections. **A**, *JN* cover that accompanied a Toolbox article covering material that was presented at two “Meet the Expert” sessions at the Society for Neuroscience meetings in 2005 and 2006 (adapted from Harris et al., 2006). **B**, Screenshot from Reconstruct, a tool for obtaining calibrated dimensions of objects reconstructed in 3D from serial thin sections (freely available for download with detailed manual at <https://synapseweb.clm.utexas.edu/software-0>). This image was generated from ongoing work in the Harris Laboratory. The windows show a calibration grid for determining the pixel size (left), a dendrite reconstructed using the Boissonnat surface tool along with a $1\text{ }\mu\text{m}$ scale cube made using the Box tool (middle), and an EM image with defined objects (right). The objects list (top middle) outputs a .csv file with calibrated dimensions that can be imported into databases for statistical analyses, and there are drawing tools and color palettes (top right) to name and illustrate traces, stamps, and other defining objects (top right) that can be superimposed on aligned images. **C**, **D**, The cylindrical diameters method to estimate section thickness for accurate volume and surface area calculations. Adapted from Fiala and Harris (2001a). **E**, **F**, Neighboring fields from the same single section (see large arrowheads pointing to the same object on the left side of the line in **F**). Adjusting synapse density in neuropil areas or volumes requires subtracting areas or volumes of objects (black dots) that nonuniformly occupy space where synapses cannot form. Adapted from Harris et al. (1992). **G**, **H**, The unbiased brick (**G**) and unbiased dendritic length (**H**) methods for 3D stereology (from Fiala and Harris, 2001b). **I**, **J**, A CA1 pyramidal cell filled with Alexa Fluor dye at scale (**I**) next to three tSEM fields montaged across the apical CA1 dendritic arbor (**J**) to illustrate the large tSEM field size relative to the typical TEM field size. **K**, The resolution of the tSEM fields ($\leq 2\text{ nm}$ pixel size) retains the same tissue elements as the original TEM fields. (**I–K** are adapted from Kuwajima et al., 2013a).

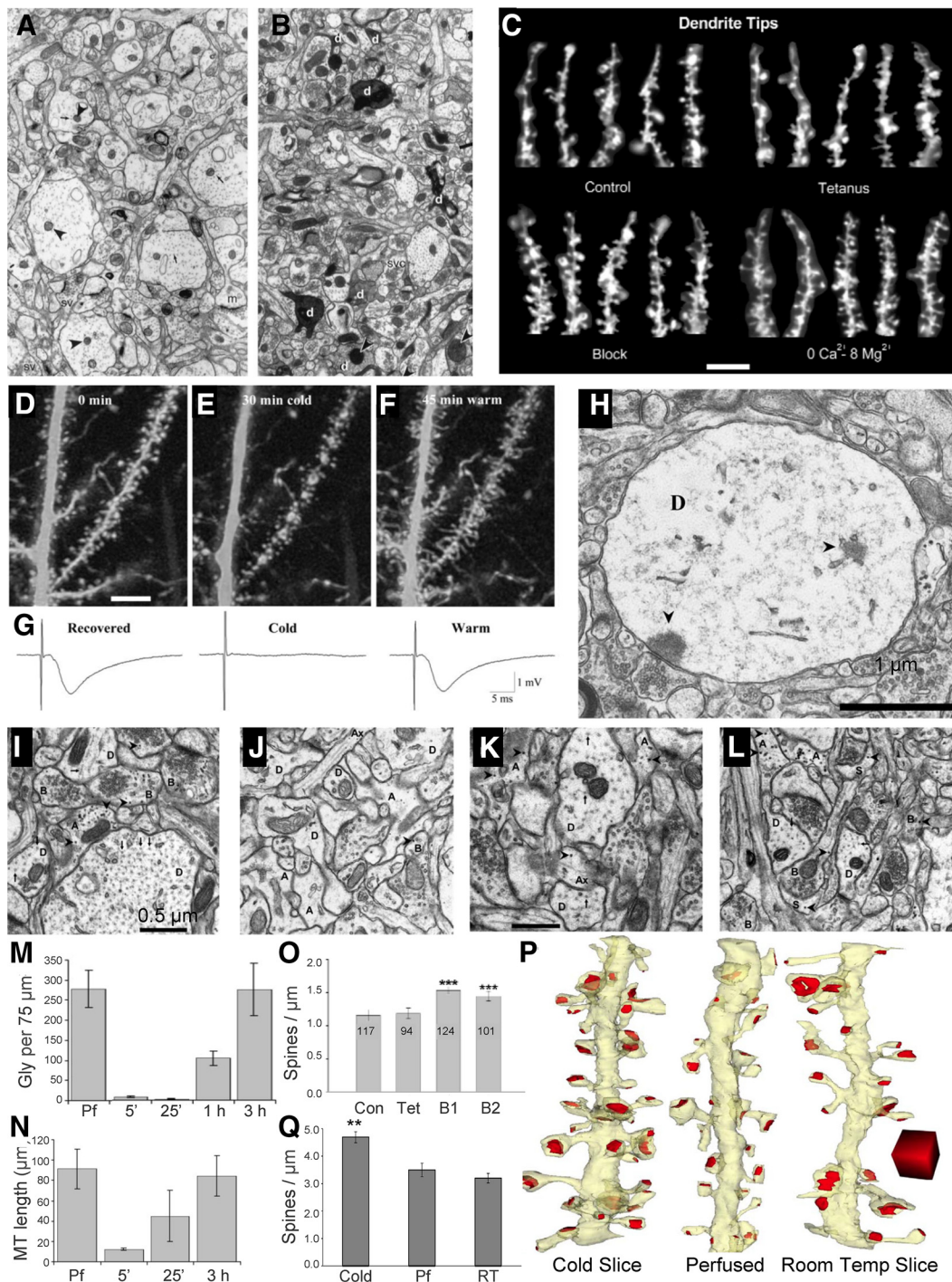


Figure 4. Establishing experimental conditions to recover quality ultrastructure in acute hippocampal slices. **A, B**, Image from a hippocampal slice that was of excellent quality and preservation (**A**), in contrast with **B**, which shows too many dark and dying processes, which was rejected for further analysis. These experiments were the first to show slicing-induced synaptogenesis. **C**, When synaptic transmission was blocked, additional synaptogenesis was triggered—the first demonstration of synaptic homeostasis in mature brain (**B** and **C** are from Kirov et al., 1999). **D, E**, Direct demonstration that once slices are recovered (**D**), chilling them to 4°C during live imaging (**E**) was sufficient to eliminate most dendritic spines and cause dendrites to swell. **F**, Upon rewarming, there is excessive proliferation of filopodia and spine-like processes. **G**, The synaptic field potential disappears upon exposure to the cold and reappears upon warming. **H**, The swollen dendrites show loss of spines and synapses and evidence of free postsynaptic densities floating in the dendritic cytoplasm (**D–H** are from Kirov et al., 2004b). **I–M**, Such observations motivated an ultrastructural investigation of the timing of recovery of hippocampal slices: perfusion fixed hippocampus (**I**), immediately after slicing (**J**), after 1 h of incubation (**K**), and 3 h later (**L**); and astrocytic glycogen was gone during the first hour (**M**) during slice incubation, suggesting that high glycolysis is needed for the neurons to recover from slices. Then small glycogen α particles began to recover and reached *in vivo* perfusion-fixed (**Pf**) levels by 3 h, suggesting that the neurons were then ready to respond normally. **N**, Microtubules were lost from dendrites (see that there is an absence of microtubules in dendritic profiles in the EM of **J**, but that they were rapidly retubulated into short segments by 25 min and reached their *in vivo* length by 3 h (**J–N** are from Fiala et al., 2003). **O**, Quantification of dendritic spines illustrated in **C** (Con, control; Tet, after tetanic stimulation; B1, aCSF with low Mg^{2+} and low Ca^{2+} ; B2, aCSF with low Mg^{2+} and low Ca^{2+} plus glutamate receptor blockers; *n* values in the bars are the numbers of dendritic tips analyzed to achieve these numbers). Note that the density is at the limit of light microscopy resolution. **P, Q**, Demonstration that hippocampal slices dissected under warmer conditions (RT, room temperature) do not have excess spinogenesis after 3 h of quiet recovery (**P**), whereas a slice prepared under ice-cold conditions triggers excessive spine density (**Q**; from Bourne et al., 2007a). Temp, Temperature. In (**A**) m = mushroom spine; chevrons are mitochondria, arrows are microtubules, sv = synaptic vesicle clumps, chevrons point to distended mitochondria. In (**H**) D = dendrite; chevrons are expanded or free-floating PSDs. In (**I–L**) A = astroglia, AX = axon, B = boutons, D = Dendrites, S = spine, chevrons = glycogen; arrows = microtubules. $^{**}p < -0.01$, $^{***}p < 0.001$.

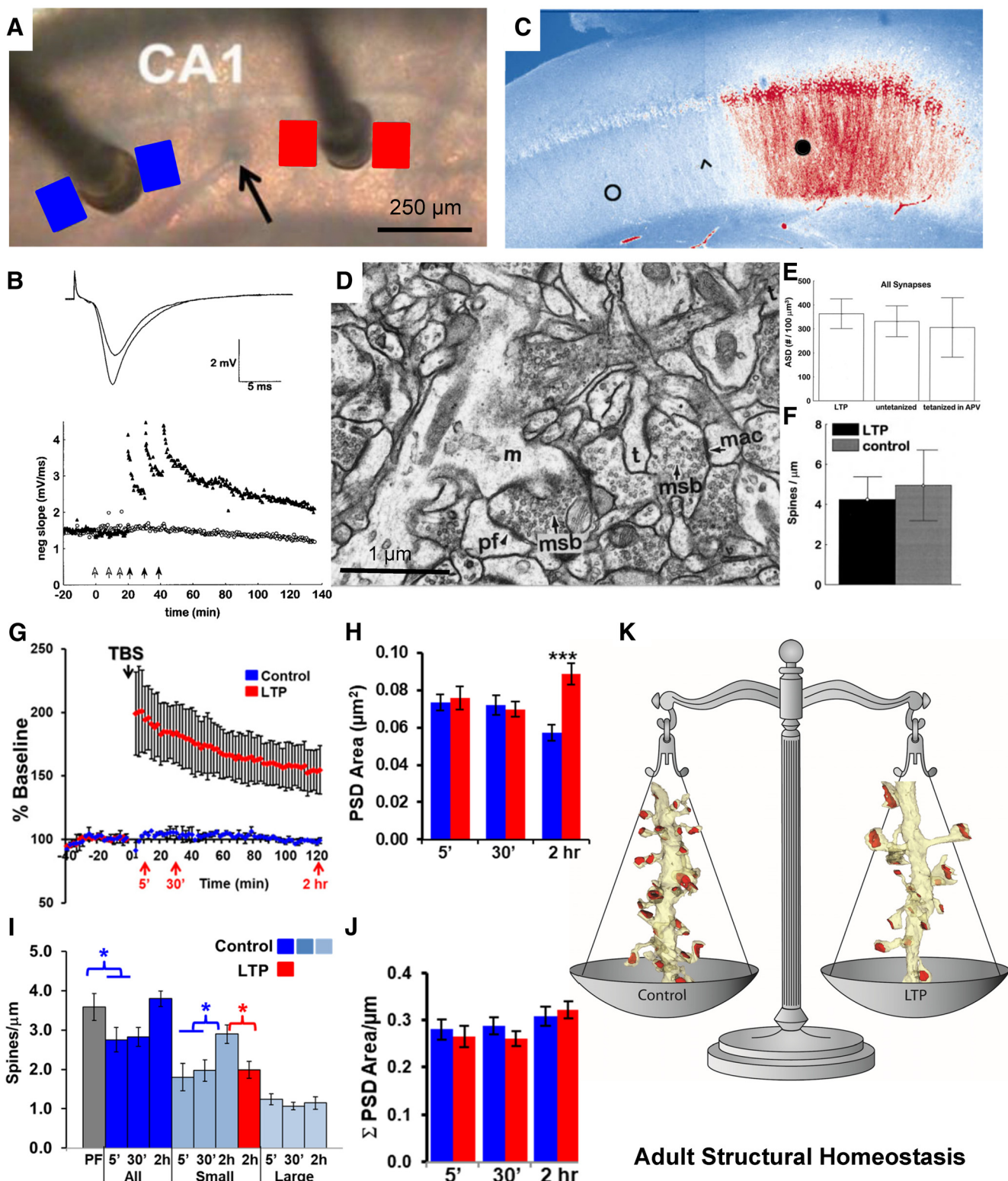


Figure 5. Ultrastructure of long-term potentiation in the young adult rat hippocampus. **A**, Positioning of stimulating electrodes and sample locations for serial EM sections from the control (blue) and LTP (red) sites. The stimulating electrode that induced LTP was alternated between the CA3 (left) and the subicular (right) side of the recording electrode (black arrow). **B**, LTP induced by three bouts of tetanic stimulation (closed arrows, 100 Hz for 1 s each), and the control side received the same number of stimuli at a slower rate that did not induce LTP (open arrows). **C**, Staining for P-CaMKII after induction of LTP at the subicular stimulating electrode (black circle) illustrates increased labeling (red) of P-CaMKII relative to the control stimulation site (open circle). The arrowhead indicates the approximate location of the recording electrode, and the scale is the same as in **A**. Adapted from Ouyang et al. (1997). **D**, Illustration of the excellent brain slice ultrastructure that can be obtained from adult hippocampal slices. **E, F**, Examination of such slices revealed that adjusted synaptic density (ASD; **E**) and spines per micrometer (**F**) were not altered by LTP induced by tetanic stimulation **B** and **D–F** were adapted from Sorra and Harris (1998). **G–I**, When LTP was induced with theta burst stimulation (**G**), and the PSD area of synapses enlarged (**H**), while the increase in small-spine density seen under control conditions was absent (**I**). **J, K**, Consequently, the total PSD area after LTP induction was similar to that in control conditions (**J**), resulting in a homeostatic balance in total synaptic weight per unit length of dendrite (**K**). **A, B, G, and H** are adapted from Bourne and Harris (2011); **I** is adapted from Bell et al. (2014). msb = multisynaptic bouton. (**D**) m = mushroom spine, pf = perforated PSD, msb = multisynaptic bouton, mac = macular PSD, t = thin spine; **p* < 0.05; ****p* < 0.001.

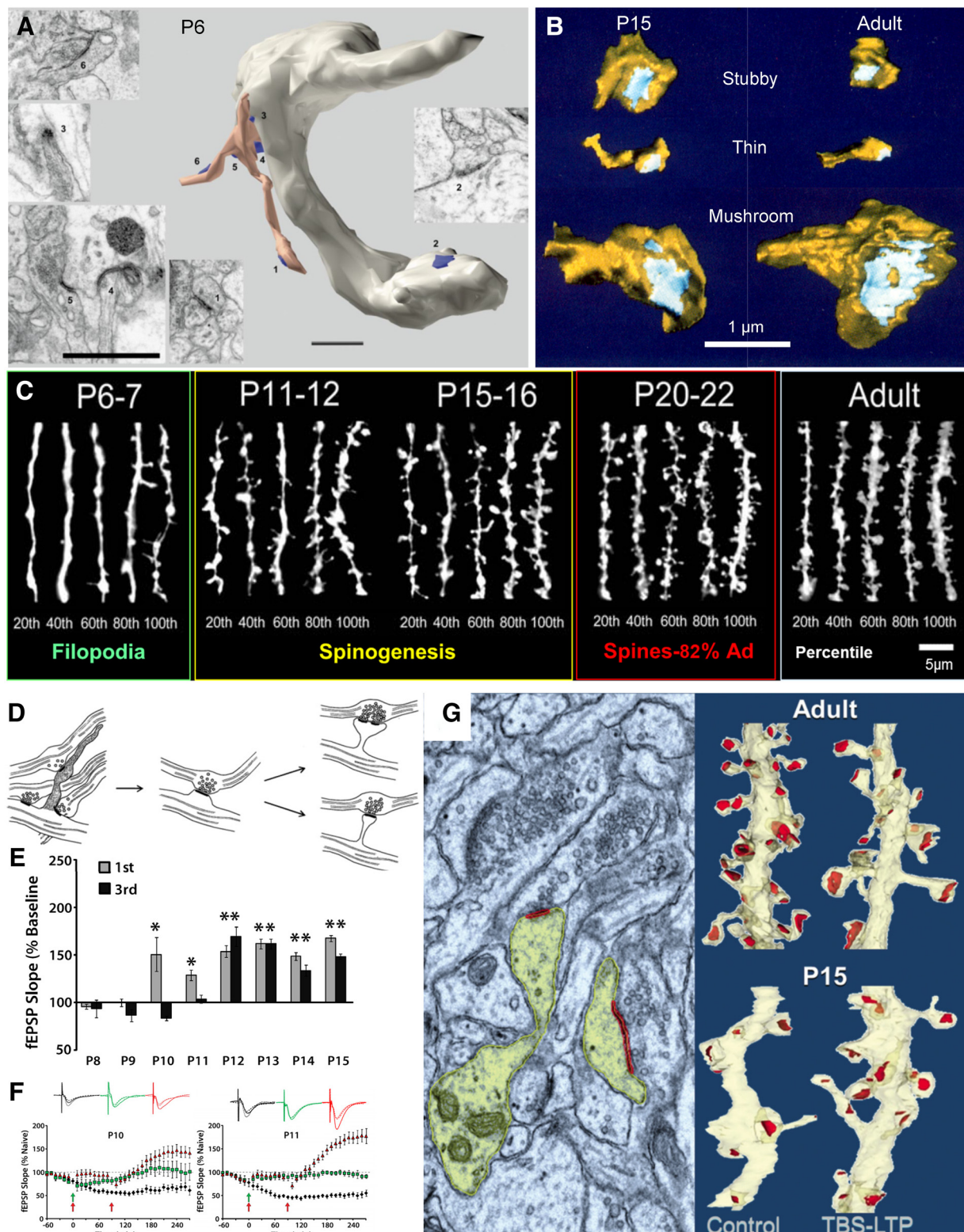


Figure 6. Synaptogenesis and the onset of LTP. **A**, EM sections and reconstruction of a varicose dendritic segment from CA1 stratum radiatum at P6. Multiple synapses (blue) are seen: one (2) is on the dendritic shaft and several are present near the tips and surrounding the base of a branched filopodium (peach colored). Adapted from Fiala et al. (1998). **B**, Dendritic spines of multiple shapes occur at both P15 and in young adults (P60–P70). From Harris et al. (1992). **C**, Confocal images of oblique dendrites from CA1 pyramidal cells in stratum radiatum, ranked by spine (protrusion) density across developmental ages compared with young adults (percentiles from 20 to 100 beneath each set of five dendrites). Adapted from Kirov et al. (2004a). By P20–P22, this density reaches ~82% of the adult level (Ad). **D**, Model of spine outgrowth during development. Adapted from Harris (1999). **E**, Developmental onset of short-term potentiation (first hour) and late-phase LTP (third hour). **F**, At P10 and P11, a second bout of TBS (second red arrow) will induce late-phase LTP if sufficient time passes between the bouts, compared with slices that receive just one bout by TBS (green arrows and waveforms) or slices that undergo test pulse-induced depression (black waveforms and symbols). **G**, At P15, TBS induction of LTP produces new dendritic spines, the left side is colorized electron micrograph (yellow, dendrite and spine heads; red, postsynaptic density), and the right side is 3D dendritic segments from young adults (top) compared with P15 (bottom) that received control or TBS stimulation. From Watson et al. (2016). (A): Numbers 1, 3–6 match EMS of synapses on the branched filopodium. *p < 0.05, **p < 0.1.

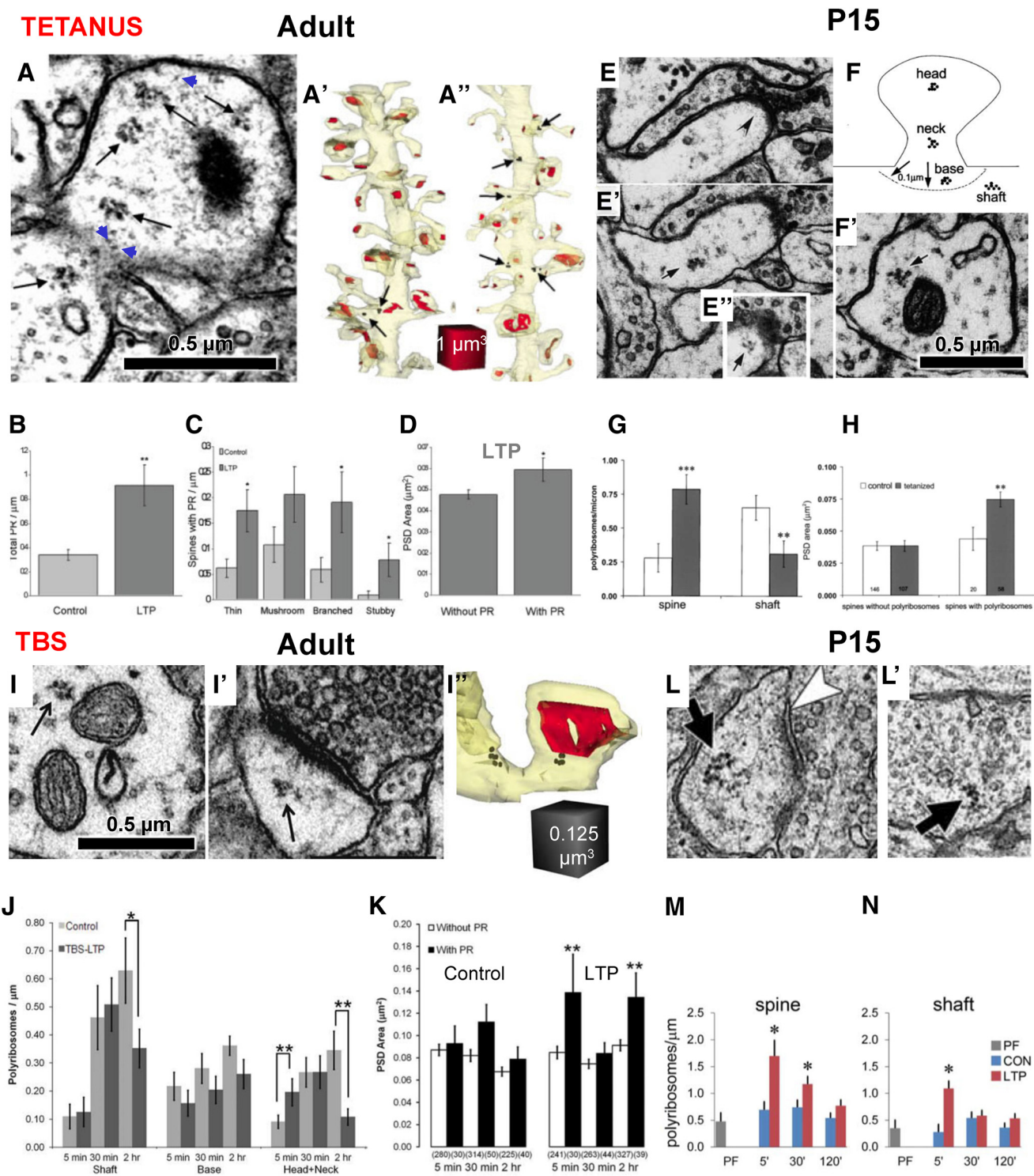


Figure 7. Effects of LTP on the distribution of polyribosomes. **A–D**, Polyribosomes in adult hippocampal areas CA1. **A**, A dendritic spine head in adult hippocampal area CA1 with polyribosomes (black arrows) and putative monosomes (blue arrows). **A'**, **A''**, 3DEM reconstructions of a representative dendrite (pale yellow) with PSDs (red) showing the positions of polyribosomes (black arrows) after control (Con) stimulation (**A'**) and after induction of LTP with tetanic stimulation (**A''**). **B**, **C**, Quantitative analysis showed that 2 h after tetanus, PR numbers were increased along the dendrites (**B**), and in dendritic spines of every shape (**C**). **D**, In addition, the synaptic surface area measured across the postsynaptic density on spines with polyribosomes was elevated 2 h after tetanus administration (**D**). **A–D** are adapted from Bourne et al. (2007b). **E–H**, Polyribosomes in P15 hippocampal areas CA1. **E–E'**, Serial EM sections through a dendritic spine show two polyribosomes (arrows) and the PSD (chevron in **E**). **F**, Schematic of identified polyribosome locations in the dendritic spines. **F'**, Polyribosomes in dendritic shaft. **G**, 2 h after LTP was induced by tetanic stimulation, more dendritic spines contained polyribosomes, whereas the neighboring dendritic shafts contained fewer polyribosomes. **H**, Spines containing polyribosomes had larger synapses. **E–H** are adapted from Ostroff et al. (2002). **I**, Polyribosome in an adult dendritic shaft. **I'**, **I''**, Polyribosome in an adult dendritic spine (**I''**); 3DEM reconstruction of spine is shown in **I'**. **J**, Distribution of polyribosomes in the shaft, spine base, and spine heads or necks at varying times after TBS induction of LTP. **K**, Synapse (PSD) surface areas at different times after TBS in adult area CA1. From Bourne and Harris (2011). **L**, **L'**, Polyribosomes in a P15 dendritic spine head (**L**) and (**L'**) dendritic shaft. **M**, **N**, Relative to perfusion fixed (PF) P15 hippocampus, control test pulses had no significant effect on polyribosome distribution among dendritic spines or shaft. Induction of LTP at P15 showed a rapid increase on polyribosomes in spines at 5 min, lasting for 30 min, while the elevation lasted only 5 min in the dendritic shafts. Ostroff et al. (2018).

spines form (Fig. 6G; Watson et al., 2016). Thus, in contrast to adult rat hippocampus, where synapse enlargement is balanced by stalled spine outgrowth, LTP enhances synaptogenesis in favor of circuit production during development. It remains to be determined whether species- and strain-dependent differences in LTP onset between mice, and in rats, can be accounted for by variance in the onset age of spinogenesis (Ostrovskaya et al., 2019).

The next big question was to determine what dendritic resources limit total synapse enlargement and number. Local protein synthesis is an important resource for synapse enlargement and spine outgrowth. Ribosomes are an ultrastructural signature of local protein synthesis. Single ribosomes, monosomes, are abundant throughout neurons but are not as readily recognized as polyribosomes (PRs) that form a string of three or more ribosomes (Fig. 7A).

When tetanic stimulation was used to induce LTP in adult rat hippocampus, dendrites contained more polyribosomes 2 h later (Fig. 7B). The polyribosomes were elevated in spines of all shapes (Fig. 7C), and spines containing polyribosomes after LTP had larger synapses than those without polyribosomes (Fig. 7D; Bourne et al., 2007). Similarly, in P15 rat hippocampus, dendritic spines acquired more polyribosomes, while dendritic shafts had fewer polyribosomes at 2 h after the induction of LTP with tetanic stimulation (Fig. 7E–G; Ostroff et al., 2002). Also, as in adults, the P15 spines with polyribosomes had larger synapses than those without polyribosomes after tetanus-induced LTP (Fig. 7H).

When TBS was used to induce LTP in adult hippocampal slices, polyribosomes also dropped in the shaft at 2 h, but the elevation in spine polyribosomes lasted only 5 min (Fig. 7I,J). Polyribosome frequency dropped below control levels by 2 h after the induction of LTP, as more spines formed and acquired polyribosomes during the control stimulation (Fig. 7J; Bourne and Harris, 2011). In addition, synapses were larger on dendritic spines that contained polyribosomes at both 5 min and 2 h after the induction of LTP by TBS in adult hippocampus (Fig. 7K; Bourne and Harris, 2011).

TBS-induced LTP also differed from tetanus-induced LTP at P15. As in adults, the TBS-induced elevation of polyribosomes at P15 occurred 5 min after LTP induction and declined thereafter (Fig. 7L,M; Ostroff et al., 2018). Furthermore, there was an elevation in shaft polyribosomes that was not sustained past the 5 min time point, and, in contrast to tetanus-induced LTP, there was no difference in polyribosome frequency in either the spines or the shafts at 2 h after TBS (Fig. 7M,N; Ostroff et al., 2018). Together, these results suggest that the pattern of stimulation used to induce LTP recruits local protein synthesis that requires polyribosomes at different times. Future work is needed to determine whether monosomes, which synthesize different proteins from polyribosomes, are also recruited at different times post-tetanus administration or post-TBS.

Another limited resource that could limit synapse enlargement and number is smooth endoplasmic reticulum (SER). SER is the largest internal membrane system, extending throughout the entire neuron. It controls both global and local lipid synthesis, protein trafficking, calcium, signaling to the nucleus, and more. Our third cover on the *Journal of Neuroscience* was a complete reconstruction of the SER illustrating the connection between the shaft SER and that in a dendritic spine (Fig. 8A; Spacek and Harris, 1997). Most spines in hippocampal CA1 stratum radiatum lack SER (Fig. 8B); however, those that contain a tubule of SER (Fig. 8C) or a well defined spine apparatus (Fig. 8D) have larger synapses. Some spines contained polyribosomes (Fig. 8E),

but it was quite rare for a single spine to contain both polyribosomes and SER, perhaps suggesting that local protein synthesis of cytoplasmic proteins occurs at different times than SER-mediated processes. Clearly, both subcellular constituents are dynamically regulated across spines. Furthermore, at 2 h after the induction of LTP, synapses on spines lacking polyribosomes and SER were 0.6% larger, whereas synapses on PR-containing spines showed a 4% increase. In addition, synapses on spines with SER showed a whopping 11% increase in postsynaptic density (PSD) area relative to control (Fig. 8F). These effects were present across all spine sizes, and thus were not limited by the surface area of the spine head, but rather by the availability of subcellular resources of polyribosomes and SER.

The distribution of dendritic spines along the dendritic shafts is not uniform (Fig. 8G). Initially, we discovered that more SER occurred where spine density and size were greatest along a dendrite, as though it was providing local resources to sustain a constant amount of synaptic input (Fig. 8H–J; Spacek and Harris, 1997). This finding spurred functional analyses in cultured neurons, where complex ER with greater volume produced slower trafficking of membrane and proteins, leading to ER exit sites (Cui-Wang et al., 2012). This effect became more prominent as cultures aged and produced dendritic spines (Fig. 8K–M). The 1997 findings were replicated with 3DEM, which showed that the summed cross-sectional area of the SER profiles (SER complexity) was greater in regions where dendritic spines clustered (Fig. 8N–R).

We wondered whether LTP and the differential availability of SER or polyribosomes influence synaptic clustering and local homeostatic balance in spine outgrowth. We divided the dendritic segments into synaptic clusters that were defined as being bounded by asynaptic regions having no spine origins for at least 120 nm (Fig. 8S–V, blue regions; Chirillo et al., 2019). As indicated above, dendritic spine outgrowth was stalled as synapses enlarged in the 2 h after TBS-mediated induction of LTP (Fig. 5I). This stalled spine outgrowth was restricted to synaptic clusters lacking the enlarged resource-rich spines (Fig. 8V,W). Complex branched SER was also locally retained in the dendritic shafts of spine clusters having resource-rich polyribosome- or SER-containing spines. Furthermore, the total synaptic weight was greater in synaptic clusters that had the resource-rich spines than in clusters without such spines, namely, those in which spines lacked polyribosomes and/or SER (Fig. 8X). These findings suggest that resource-rich spines undergo the most enlargement, yet they share resources with their immediate neighbors, allowing local spine outgrowth.

Endosomes present a third limited resource that influences dendritic spine formation and plasticity. In our initial work, we discovered that gold particles conjugated with protein and delivered to the extracellular space were taken up into endosomal compartments following extracellular stimulation (Fig. 9A; Cooney et al., 2002). The endosomal compartments included multivesicular bodies with coated invaginations (Fig. 9B), sorting complexes (Fig. 9C), coated pits in the plasma membrane (Fig. 9D), large and amorphous vesicles (Fig. 9E), tubules, and coated vesicles (Cooney et al., 2002). Small vesicles and SER contained no gold particles, providing strong evidence that these compartments are not part of endosomal recycling (Fig. 9F). At P15, ~50% of dendritic spines had one or more endosomal, vesicular, or SER compartments (Fig. 9G). The fraction of spines with endosomes peaked at P21, an age when spinogenesis is also maximal in this hippocampal CA1 region (Fig. 9H).

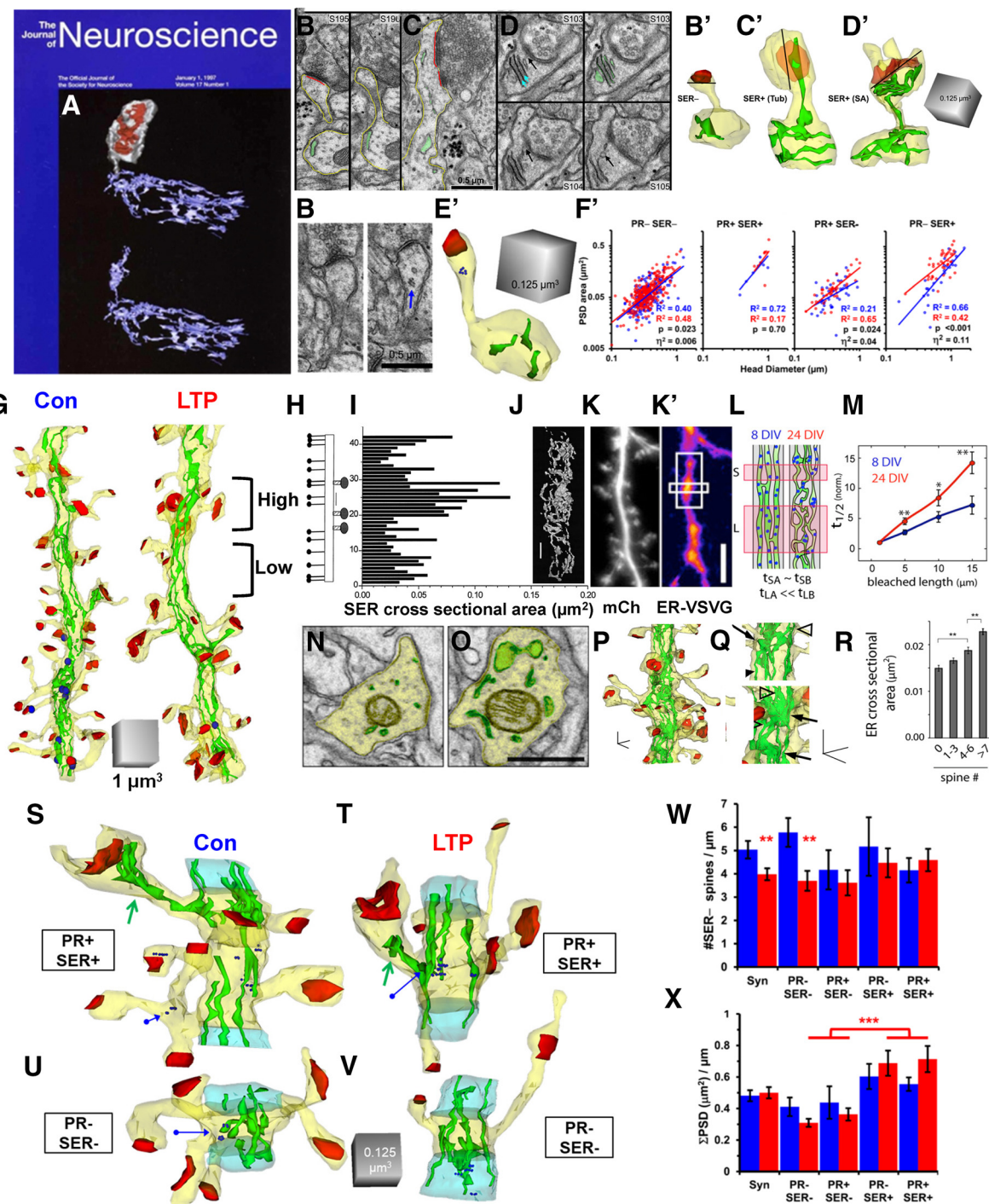


Figure 8. Effects of SER and PRs on synaptic plasticity and homeostasis. **A**, Three-dimensional reconstruction of a large dendritic spine (gray), with a large, irregular, perforated synapse (red) and its spine apparatus, which is continuous with the network of SER in the dendritic shaft. **B–D'**, Serial EM sections and three-dimensional reconstructions of spines: a spine without SER (**B**, **B'**), a spine with a simple tubule of SER (**C**, **C'**), and a spine with a spine apparatus (**D**, **D'**). The lines in the 3D reconstructions illustrate how the head diameter was measured at its widest point. **E**, **E'**, Serial sections and 3DEM illustrating a polyribosome in an adult dendritic spine head (blue arrow). **F**, Synapse enlargement after LTP, controlled for head diameter relative to subcellular composition. **G**, Fully reconstructed dendritic segments from adult rat hippocampal slices under control (Con) and LTP conditions, illustrating regions of high and low spine density. **H**, **I**, In adult hippocampus *in vivo*, the schematic shows the locations of small and large spine origins (**H**), which match the section locations indicated in **I**, where the y-axis is the section number and the x-axis charts the total cross-sectional area of SER in the dendritic shaft on each segment. **J**, 3DEM of the shaft SER that is graphed in **I**. **K–L**, In cultured hippocampal dendrites, we showed that where the dendritic shaft SER was more complex in structure, trafficking was slowed and provided regions for cargo exit to deliver resources to synapses. **M**, The length of the complex ER exit sites increased with age. **N–R**, Regions of SER complexity gave rise to more dendritic spines in adult hippocampus. **S**, **T**, Synaptic clusters having spines with large synapses and resource rich spines containing polyribosomes or SER (PR⁺, SER⁺) in the control (Con) and LTP conditions. **U**, **V**, Synaptic clusters lacking resource-rich dendritic spines (PR⁻, SER⁻) in the control and LTP conditions. **W**, The homeostatic stalling of spine outgrowth was restricted to synaptic clusters lacking resource-rich spines. **X**, In contrast, regions of the dendritic segment that had resource-rich spines had a greater total synaptic weight, measured as the summed PSD area per length of cluster segment.

A and **H–J** are adapted from Spacek and Harris (1997); **B–G** and **S–X** are adapted from Chirillo et al. (2019); **K–R** are adapted from Cui-Wang et al. (2012).

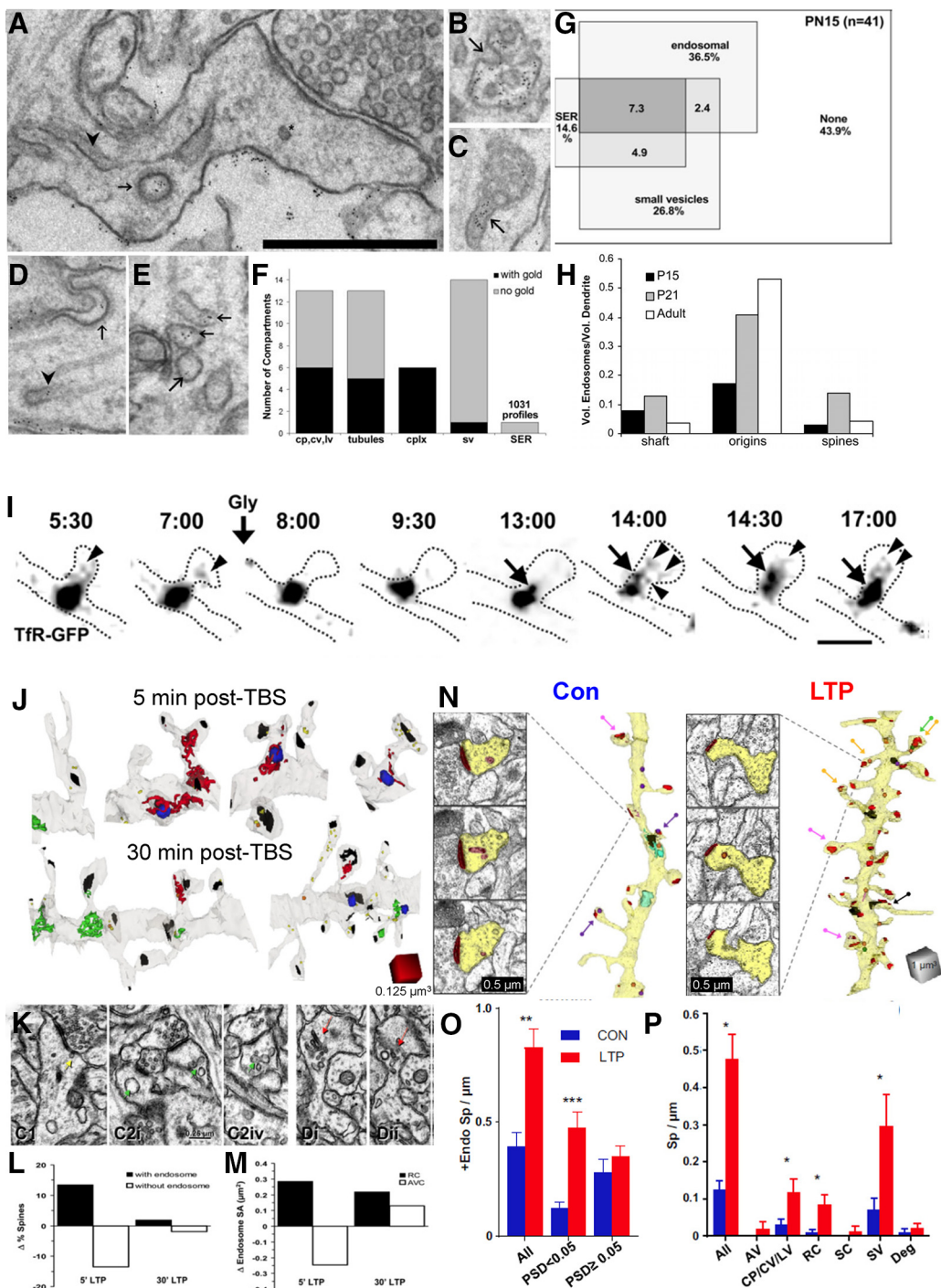


Figure 9. Endosomes move into dendritic spines in response to stimulation. **A–E**, Electron micrographs from a P21 hippocampal slice that was first given tetanic stimulation, followed by 900 pulses in the presence of bovine serum albumin conjugated to gold particles. **A–E**, Postsynaptic endocytosis was demonstrated by gold particles taken up from the extracellular space into large vesicles (**A**), invaginations into multivesicular bodies (**B**), sorting complexes with tubules (**C**), coated pits (**D**), and amorphous vesicular clumps (**E**). **F**, Quantification of gold particles in coated pits (cp), tubules, and sorting complexes (cplx). Note that particles were rarely seen in small presumably exocytic postsynaptic vesicles (sv), and never in SER profiles. **G**, Relative distribution of endosomal compartments occupying dendritic spines at postnatal day 15 of a total of 41 dendritic spines. **H**, are adapted from Cooney et al. (2002). **I**, Time-lapse imaging of recycling endosomes mobilized into spines after glycine stimulation. Neurons expressing GFP-tagged transferrin receptor (TfR-GFP), a classic recycling cargo, and monomeric red fluorescent protein to fill the spines, represented by the dotted line. The spines were imaged every 15–30 s before and after glycine stimulation (200 mM, 3 min). Times are indicated as minutes:seconds. Arrows indicate the movement of large endosomes into the spine from the shaft. Arrowheads indicate vesicles or tubules emanating from larger TfR-containing endosomes. Scale bars, 1 μm. **J**, 3DEM reconstructions of dendritic segments at 5 and 30 min after TBS illustrating endosomes occupying the shaft and spines. (PSDs are in black; red, green, and blue represent different endosomal compartments). **K**, Example dendritic protrusions with large vesicular components. **L**, Changes in the percentages of spines with endosomes after LTP induction. **M**, Change in the amount of surface area available in the endosomes. **I–M** are adapted from Park et al. (2006). **N**, Electron micrographs and 3D reconstructions of dendritic segments illustrating the increase in the number of small spines at 2 h after the induction of LTP. **O**, **P**, Increased occupancy of endosomes in small spines 2 h after LTP. **N** and **O** are adapted from Kulik et al. (2019). * $p < 0.05$; ** $p < 0.01$; *** $p < 0.001$.

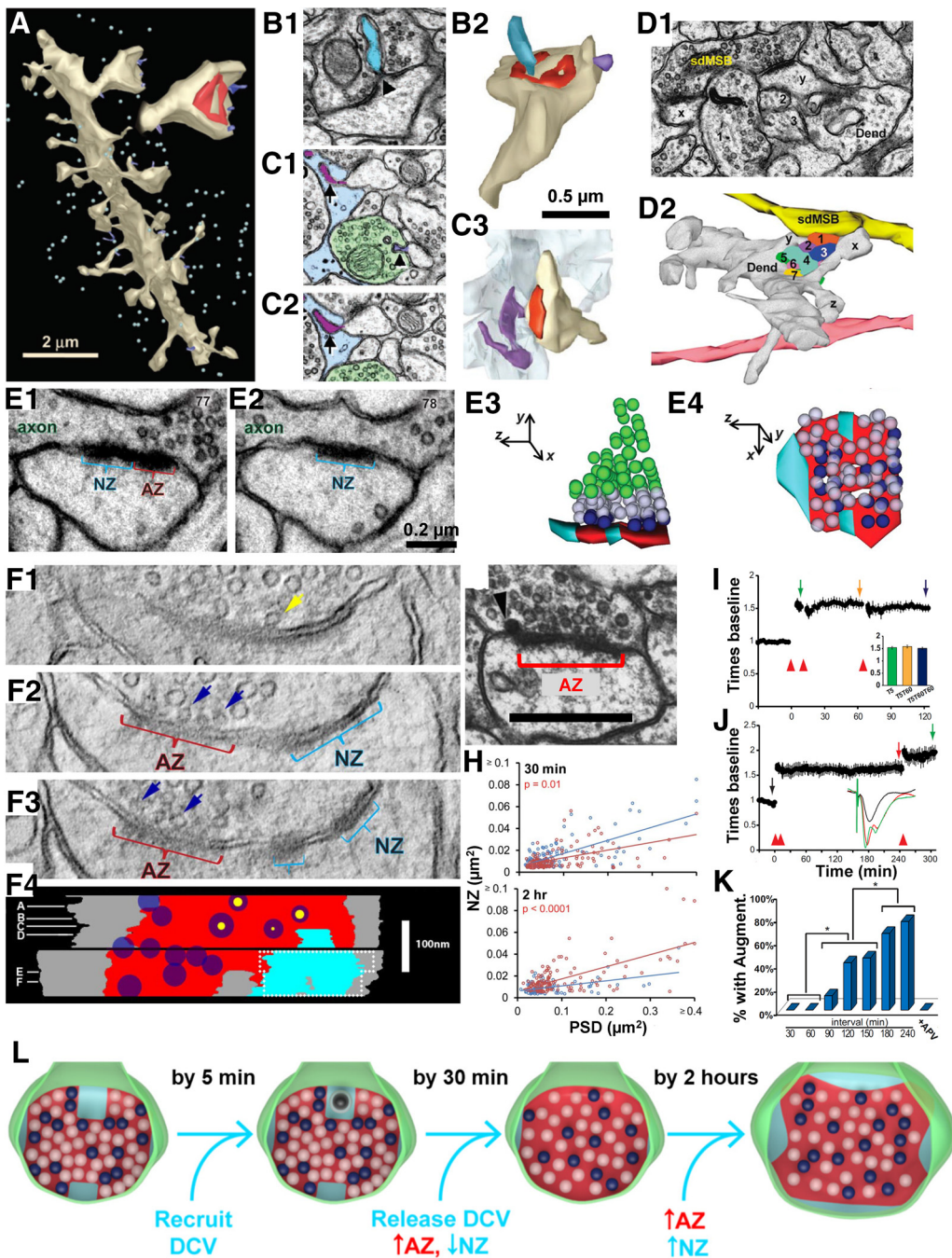


Figure 10. Dendritic spines do not split; instead spinules, perforations, branched spines, and nascent synaptic zones serve LTP and possibly underlie the advantages of spaced learning. **A–B2**, Spinules (blue) emerge from within the perforations of postsynaptic densities (red) on large dendritic spines (beige) and extend into presynaptic boutons (green in **C1**). **C1–C3**, A spinule (purple) that deeply invaginates perisynaptic astroglia (pale blue) as readily seen in 3DEM. Adapted from Spacek and Harris (2004). **D1, D2**, EM (**D1**), and 3D (**D2**) reconstruction illustrating the head of a branched spine (X) that shares the same presynaptic axon (yellow) with an unbranched spine (Y) located further up the dendrite (Dend). Seven (numbered) independent axonal processes pass between spines X and Y beneath this same dendrite multisynaptic bouton (sdMSB). The other branch of spine X (branch Z) synapses with a different axon (peach) that runs perpendicular to the yellow axon. Adapted from Fiala et al. (2002a). In panels **D1** and **D2** the numbers refer to individual axons passing between the neighboring spines. **E1, E2**, Two serial sections illustrating a nascent zone (NZ) in the PSD characterized by the absence of presynaptic vesicles (AZ is the part of the postsynaptic density across from the presynaptic active zone, with presynaptic vesicles). **E3, E4**, This organization becomes obvious in the 3D reconstructions showing the AZ (red), NZ (turquoise), docked vesicles (dark blue), vesicles within two vesicle diameters of the AZ (white), and the presumptive reserve pool of vesicles (green). **F1–F3**, Virtual thin sections (3 nm) through the AZ and NZ of two 150 nm sections through a synapse (**F1–F3**), which is reconstructed in **F4** (colors same as **E**, plus yellow arrow in **F1** and yellow dots in **F4** indicate the extent of the opening of the docked vesicle). **G**, Dense-core vesicle “inserting” at the edge of an AZ. **H**, NZs decrease in frequency and size by 30 min after LTP (red) relative to control (blue), but fully recover and enlarge by 2 h after the induction of LTP with TBS (red LTP is above blue control). **I**, When LTP is fully saturated by TBS (delivered at times indicated by red arrowheads), delivering TBS 5 min or up to an hour later produces no further potentiation (quantified in inset). **J**, When the third TBS is delivered 4 h after LTP saturation, additional LTP can be produced. **K**, About 20% of slices shows augmentation of LTP if the third TBS is given 90 min later; the relative frequency of augmenting LTP increases with time. This augmentation of LTP is blocked by APV. **L**, Model of conversion of NZ to AZ followed by the subsequent growth of NZ over the time course following LTP. The colors are the same as in **E–G** and **L**, and are adapted from Bell et al. (2014); **H–K** are adapted from Cao and Harris (2014). DCV, Dense-core vesicle.

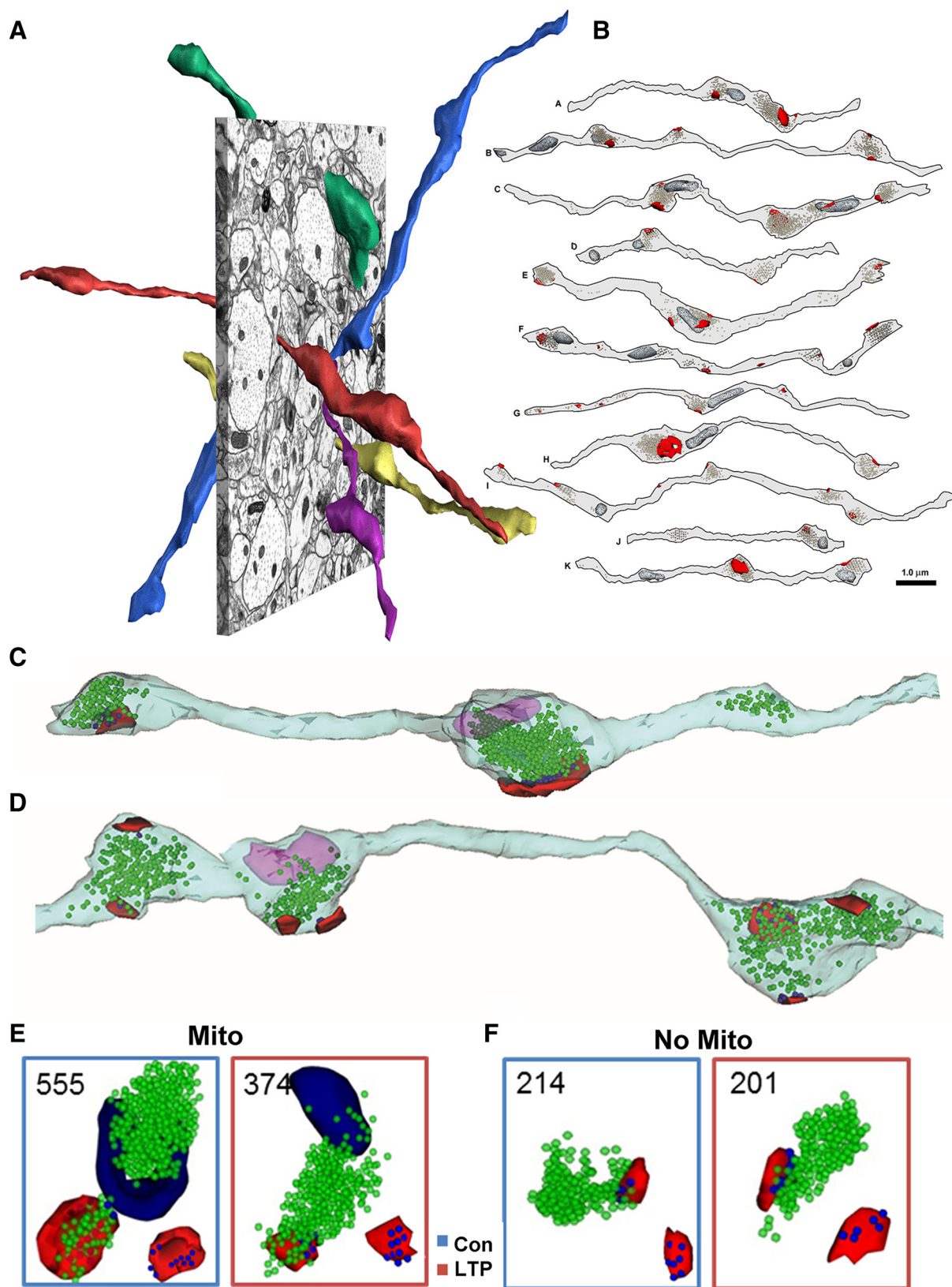


Figure 11. Diverse composition of vesicles and mitochondria (Mito) in presynaptic boutons along CA3 → CA1 axons, and their response to LTP. **A**, 3DEM of Schaffer collateral axons illustrating their nonparallel trajectories. **B**, Illustration showing that only ~50% of the presynaptic boutons contain mitochondria (dark gray structures) and synapses (red). **A** and **B** are adapted from Shepherd and Harris (1998). **C, D**, A reconstructed axon from the control condition (**C**) and an axon 2 h after LTP (**D**) illustrating the obvious drop in vesicles (axon, pale blue; vesicles, green spheres; mitochondria, fuchsia; PSDs, red; adapted from Bourne et al., 2013). **E**, Representative vesicle composition in presynaptic boutons containing mitochondria (dark blue) from the control (blue box) and LTP (red box) conditions. **F**, Representative vesicle composition in presynaptic boutons lacking mitochondria. For **E** and **F**, green spheres are vesicles in the reserve pool, and dark blue spheres are docked vesicles superimposed over the red PSDs. Adapted from Smith et al. (2016).

These observations led our collaborators to investigate the dynamics of endosomal compartments in cultured neurons. When the cultures were exposed to glycine, they produced LTP and recruited endosomes into dendritic spines for at least 20 min (Fig. 9*I*; Park et al., 2006). In P15 hippocampal slices, TBS-induced LTP recruited amorphous vesicular clumps into dendritic spines immediately after the induction of LTP; this effect returned to control levels by 30 min post-TBS (Fig. 9*J–M*). Curiously, at 2 h post-TBS many small spines had formed and had more endosomes (Fig. 9*N–P*; Kulik et al., 2019). These findings suggest an important role for endosomal structures in spineogenesis and the maintenance of new dendritic spines following TBS-induced LTP.

Prominent in the literature is the idea that dendritic spines can split to form new spines. One step in this process is thought to involve the insertion of a small protrusion called a spinule to divide the presynaptic bouton. This idea was dispelled by three-dimensional quantitative analyses of spinules (Fig. 10*A*; Spacek and Harris, 2004). The results showed that instead of “splitting” presynaptic axons, spinules are encapsulated by their presynaptic axons; furthermore, the cytoplasmic side of the encapsulating membrane has a coat (Fig. 10*B*). Spinules can also be engulfed by nonsynaptic regions of neighboring axons, perisynaptic astroglia (Fig. 10*C*), and, occasionally, other dendrites. Together, these observations suggest that spinules are involved in an active process of transendocytosis where integral membrane ligands can be transported between cells.

The spine-splitting hypothesis also proposes that dendritic spines can split into two or more spines sharing the same presynaptic axon. Two key findings argue against this hypothesis. First, different heads of branched dendritic spines, the presumed splitting intermediaries, rarely share the same presynaptic axon—in fact, this configuration has not yet been seen in area CA1 (Sorra et al., 1998; Fiala et al., 2002). This finding suggests that branched spine heads form independently to synapse with separate axons (Sorra et al., 1998; Fiala et al., 2002). Second, when neighboring spines on the same dendrite share the same presynaptic bouton, multiple long processes, including other axons, pass between the spines (Fig. 10*D*). To allow an existing spine to split, the intervening processes would have to disconnect from synapses along their hundreds of micrometers of length, pull away, let the spine split, and then rethread their way back through the neighboring spines, which is impossible in the time frame of normal plasticity! Thus, as argued further in the original article, spines branch, but preexisting synapses do not split.

Since the magnitude of LTP does not change between 30 min and 2 h post-TBS, we were curious to know whether there might be a structural basis for understanding the growth of the PSD first detected at 2 h, despite no further potentiation in the response. Long ago, we discovered a region of the postsynaptic density that was apposed to a presynaptic site but had no docked or reserve presynaptic vesicles (Fig. 10*E*). This region was originally referred to as a vesicle-free transition zone (Spacek and Harris, 1998), but later we discerned this region to be a nascent zone that is remarkably responsive to plasticity (Bell et al., 2014). Tomographic analysis of 3 nm virtual sections confirmed that no synaptic vesicles were hidden within the depths of serial sections through a nascent zone (Fig. 10*F*). This nascent zone is distinct from the so-called perforated postsynaptic density where the density is divided by translucent cytoplasm and presynaptic vesicles are docked across from the PSD on both sides of the perforation (Fig. 10*A,B*). Dense-core vesicles could be observed docking in the presynaptic region where a nascent zone most likely had

previously occurred, at the edge of an active zone (Fig. 10*G*; Sorra et al., 2006). These dense-core vesicles are attached to presynaptic vesicles via spicules and are recruited to the presynaptic boutons within 5 min after TBS induction of LTP (Bell et al., 2014). By 30 min, presynaptic vesicles were added, and the postsynaptic nascent zones disappeared or shrank, but the size of the whole PSD had not yet enlarged (Fig. 10*H*, top). By 2 h, the nascent zones reappeared, accounting for most of the PSD enlargement detected by 3DEM at this time (Fig. 10*H*, bottom; Bell et al., 2014).

The plasticity of nascent zones raised another important question. If PSD enlargement is not the basis for sustaining LTP, perhaps it prepares the synapse for subsequent plasticity. To test this hypothesis, we prepared hippocampal slices and subjected them to repeated bouts of TBS at various intervals (Cao and Harris, 2014). Two TBS episodes were delivered 5 min apart to demonstrate that LTP was indeed saturated. If a third episode was delivered an hour later, the potentiation remained unchanged, it was not augmented (Fig. 10*I*); but when the third episode was delivered after 4 h, LTP was reliably augmented (Fig. 10*J*). Indeed, when many slices were tested, augmentation failed in all cases if the delay was 30–60 min, but could occur after a 90 min delay (Fig. 10*K*). The augmentation of LTP was blocked by an NMDA receptor antagonist, suggesting that it uses the same underlying mechanism as the initial LTP. These findings generated a new hypothesis about the involvement of nascent zones in producing and augmenting LTP (Fig. 10*L*). Initially, a hippocampal slice has nascent zones available from the prior experience of the animal. By 5 min after the induction of LTP, dense-core vesicles and their tethered presynaptic vesicles are recruited to presynaptic boutons. By 30 min, the dense-core vesicles merge with the presynaptic membrane and enlarge the active zone and fill the nascent zone with tethered vesicles. By 2 h, nascent zones are regenerated, thus enabling subsequent augmentation of LTP. This delay in preparation of new nascent zones could be an underlying mechanism for the advantage of spaced over massed learning.

Presynaptic axons also undergo other forms of plasticity with LTP. Three-dimensional reconstructions of axons in CA1 stratum radiatum revealed diversity among neighboring boutons, some with mitochondria, vesicles, and postsynaptic partners; but many lack mitochondria and/or postsynaptic partners, while others contain only a mitochondrion or vesicles, but not both (Fig. 11*A,B*; Shepherd and Harris, 1998). The overall number of docked and reserve vesicles are decreased in the presynaptic boutons at 30 min and 2 h after the induction of LTP (Fig. 11*C,D*; Bourne et al., 2013). The drop in vesicles at 2 h occurs predominantly in boutons that contain mitochondria (Fig. 11*E,F*; Smith et al., 2016). Preliminary findings suggest that the reduced pool of presynaptic vesicles serves to enlarge the presynaptic bouton, perhaps also in preparation for later augmentation of LTP (Kirk et al., 2018).

Perisynaptic astroglial processes might also influence the plasticity of synapses. Astroglial processes occur at the interface of ~50% of hippocampal dendritic spines, but rarely, if ever, completely surround the axon–spine interface (Fig. 12*A–C*; Ventura and Harris, 1999; Witcher et al., 2007). When new small dendritic spines form during slice recovery and control test pulses, they are less likely than larger stable spines to have perisynaptic astroglia at their perimeters (Witcher et al., 2007). In human epilepsy, dendritic spines are lost, and presynaptic axons crowd the remaining large, multisynaptic spines (Fig. 12*D*). Perisynaptic astroglial processes withdraw from these multisynaptic spines (Witcher et al., 2010). Whether astroglial processes respond dif-

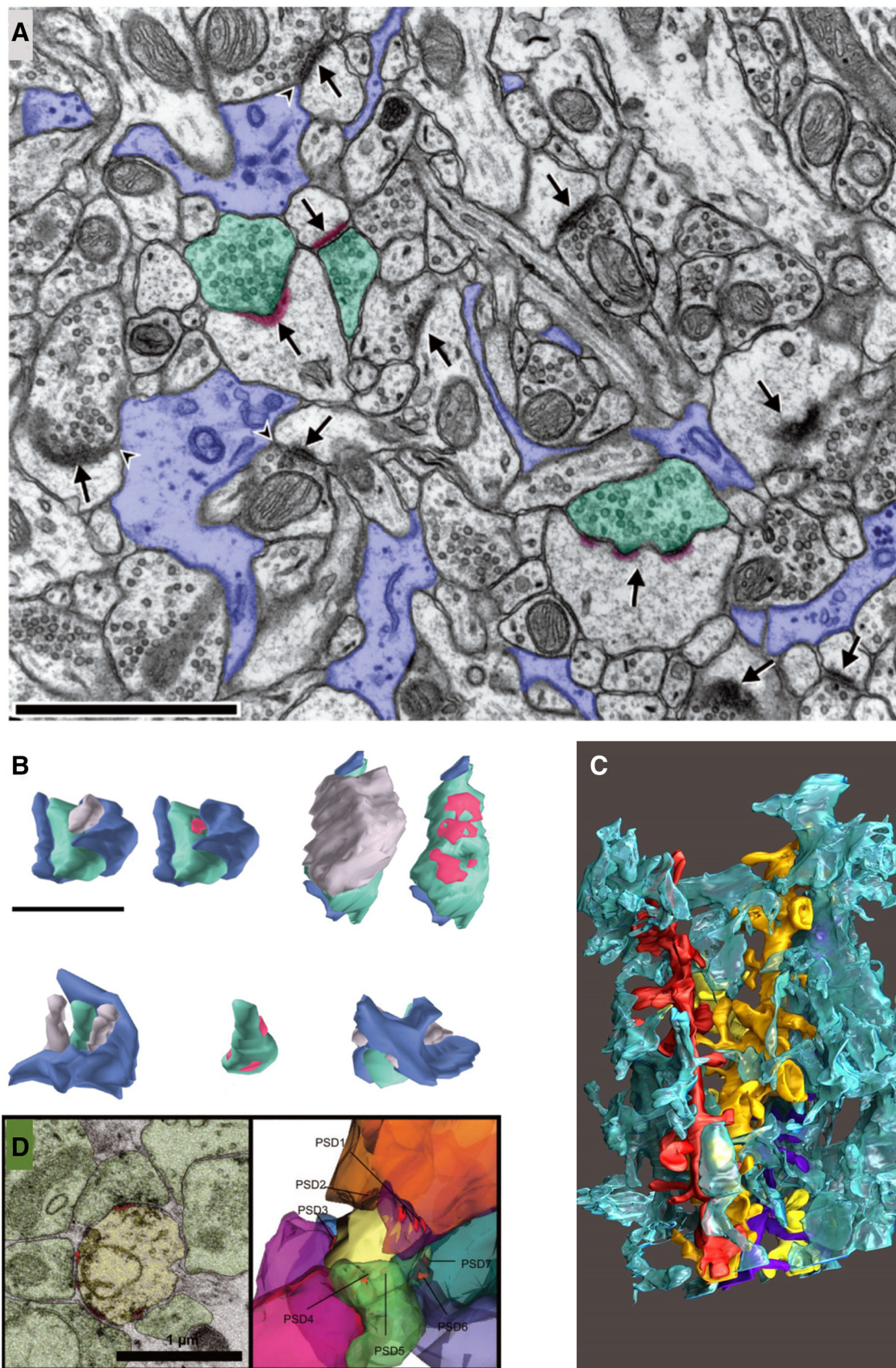


Figure 12. Perisynaptic astroglial processes. **A–C**, Electron micrographs (**A**) and reconstructions (**B**, **C**) illustrate the nonuniform distribution of perisynaptic astroglial processes among synapses in mature hippocampal area CA1. Glial processes are lavender in **A** and **B**, and turquoise in **C**. Presynaptic axons are green, PSDs are red, and the postsynaptic spines are gray in **A** and **B**. Three dendrites (red, yellow, purple) are illustrated with the interdigititation of the glial processes in **C**. **D**, A multisynaptic dendritic spine, one of the few spines that remained in a surgically removed hippocampus from a patient with epilepsy. **A** and **B** are adapted from Ventura and Harris (1999); **C** is from Witcher et al. (2010).

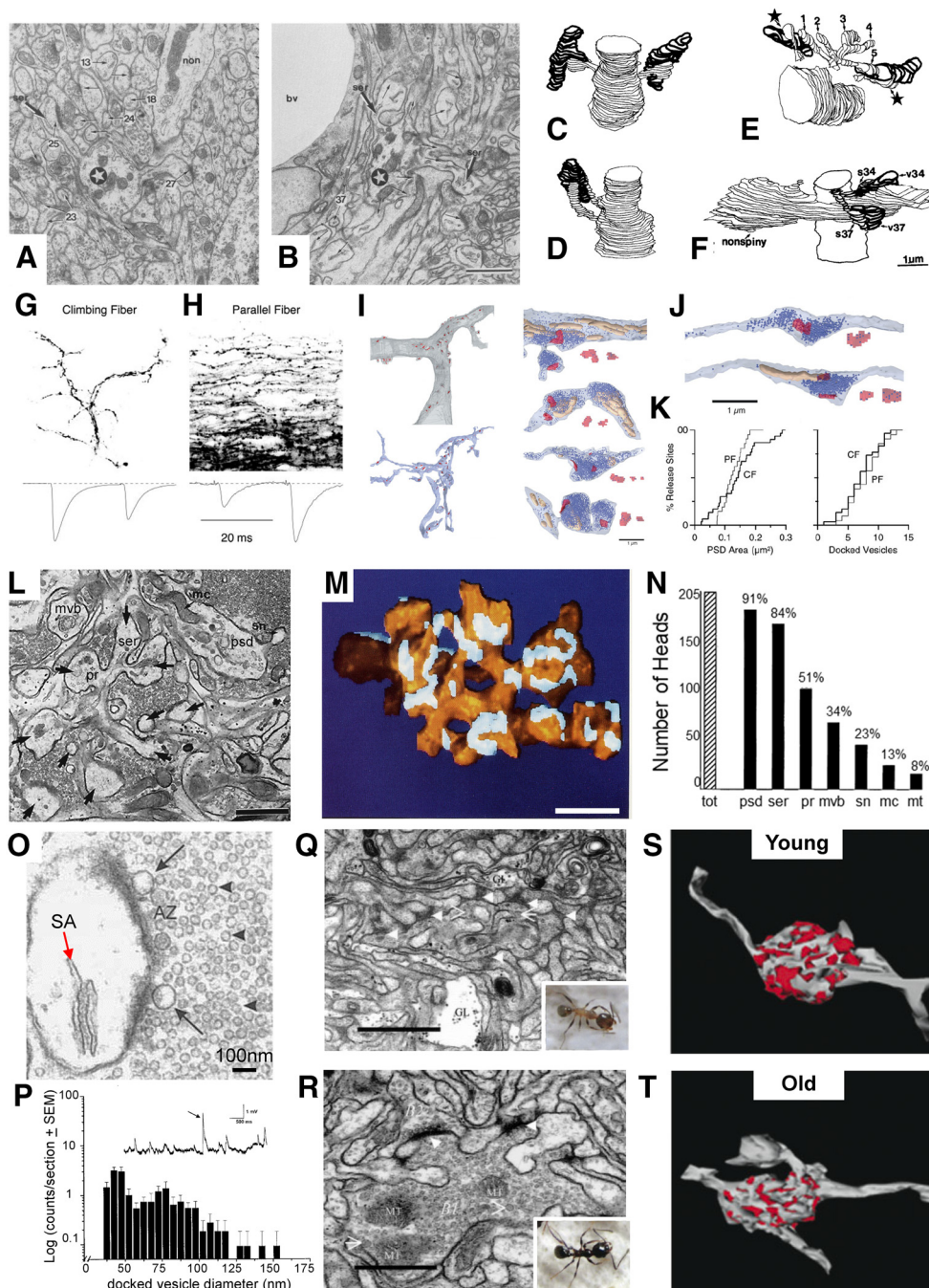


Figure 13. Diversity in spine and synapse structure from other brain regions. **A**, Purkinje cell dendrite (star) surrounded by dense neuropil in the vicinity of a nonspiny dendrite (non) from a local interneuron. **B**, Purkinje cell dendrite (star) near a small blood vessel (bv). The numbers used in panels A and B refer to individual spines that were illustrated in the original publication. **C**, Reconstructions with hidden lines on the backside removed, of two spines from the dendrite in **A** (thin lines) synapsing with two different axons (dark lines). **D**, 3D reconstruction of two neighboring spines sharing the same presynaptic axon. **E**, Five-headed spine, showing that heads 1 and 5 share their respective presynaptic boutons with different spines from the same dendrite (stars). **F**, Two spines sharing a presynaptic axon with a nonspiny dendrite. **A–F** are adapted from Harris and Stevens (1988). **G**, Biotinylated climbing fiber axons and responses showing paired-pulse depression. **H**, Filled parallel fibers with paired-pulse facilitation. **I**, 3D reconstruction of a proximal Purkinje cell dendrite (top) showing sites of synaptic contacts (red) made by the climbing fiber (blue, bottom). Panels on right show enlarged reconstructions of some of those contacts where some contain mitochondria (beige). **J**, 3D reconstruction of two parallel fibers (translucent blue) with vesicles (solid blue), mitochondria (beige), and synapses (pink). **K**, Cumulative frequencies of the number of release sites versus PSD area and the number of docked vesicles for climbing fibers (CF) and parallel fibers (PF). **G–K** are adapted from Xu-Friedman et al. (2001). **L**, Electron micrograph illustrating a section through a CA3 branched thorny excrescence (arrows) containing postsynaptic densities (psd), polyribosomes (pr), mitochondria (mc), smooth endoplasmic reticulum (ser), multivesicular bodies (mvb), and a spinule (sn). **M**, 3D reconstruction of the Thorny excrescence (yellow) in **L** with its PSDs (light blue). **N**, Relative frequencies of characteristic subcellular features in 205 reconstructed CA3 branched spine heads. **L–N** are adapted from Chicurel and Harris (1992). **O**, Head of a CA3 branched spine containing a spine apparatus (SA) and illustrating the active zone (AZ) showing docked giant clear vesicles (arrows), and small synaptic vesicles (arrowheads). **P**, Log-normalized histogram of vesicle sizes docked at 11 AZs of four reconstructed boutons. Inset shows miniature excitatory synaptic potentials recorded from these boutons where some are the small, standard size, while others reflect the fivefold greater size of the large vesicles. **O** and **P** are adapted from Henze et al. (2002). **Q–T**, EMs from the mushroom body in young and old ants (**Q**, **R**, insets), and 3D reconstructions of the boutons and synapses (**S**, **T**, red) located in the center of the EMs in **Q** and **R**. **R–T** are adapted from Seid et al. (2005). Scale bars, 1 μ m (except as indicated in **N**).

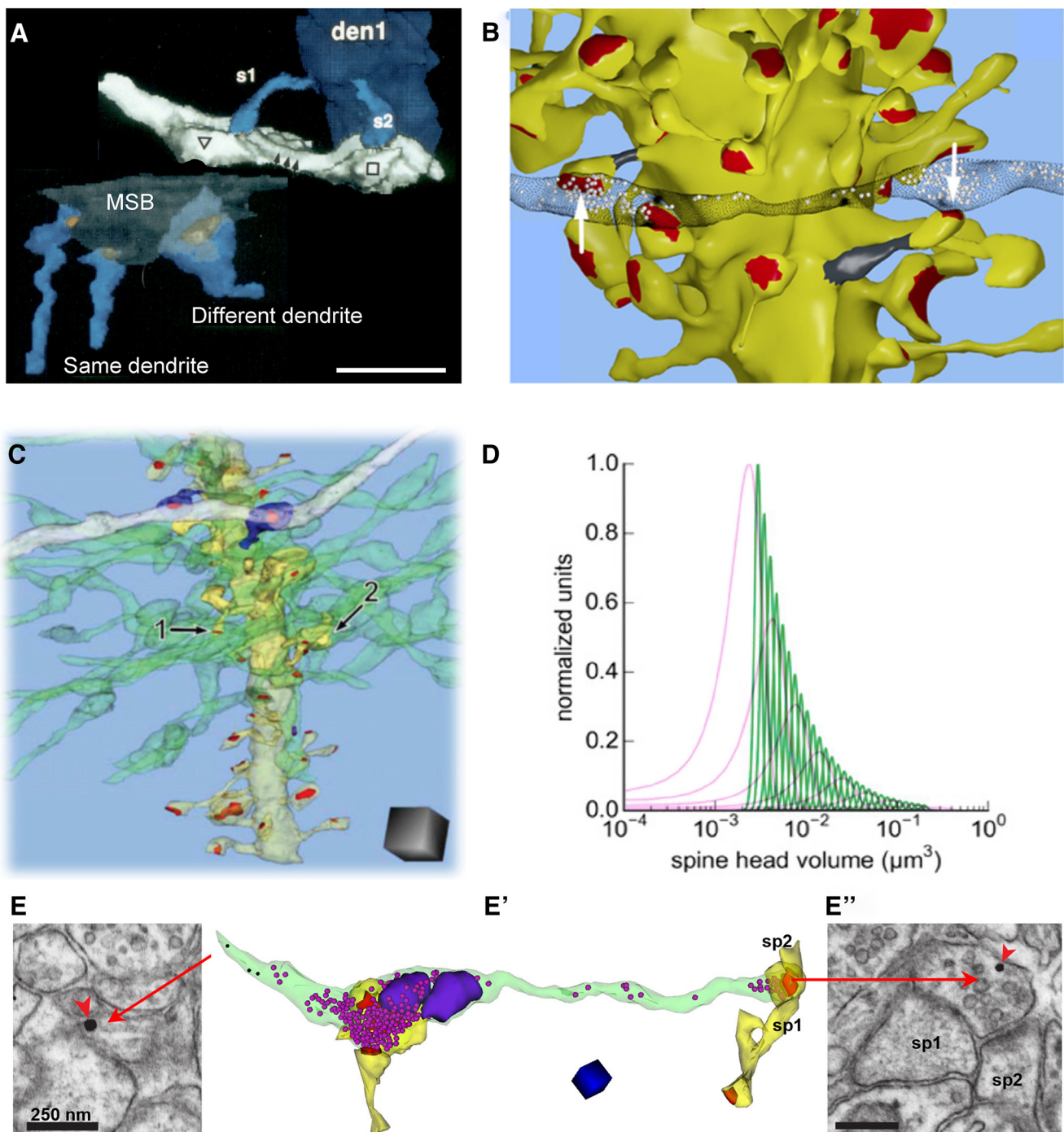


Figure 14. Understanding structural responses to coactivation of presynaptic and postsynaptic components. **A**, Two spines arising from the same CA1 dendrite and synapsing with the same presynaptic axon are more similar in size than are spines from different dendrites sharing a multisynaptic bouton (MSB). Adapted from Sorra and Harris (1993). **B**, The CA1 spine head volumes (yellow, white arrows) provided a more robust measure of precision than spine necks (gray). Scale bars: **A**, **B**, 1 μm . **B** is adapted from Bartol et al. (2015). **C**, Perforant pathway input to the middle molecular layer of the dentate gyrus, where one axon (white) is shared by two postsynaptic spines (blue). Other axons (green) synapse with different spines (e.g., 1 and 2) on the same dendrite (yellow). Scale cube is 1 μm^3 . **D**, Comparison of unique spine head volumes for dentate granule cell dendritic spines (pink) and CA1 pyramidal cell dendritic spines (green), based on information theory. **C** and **D** are adapted from Bromer et al. (2018). **E**, **E'**, New approach to labeling light-activated axons with postembedding immunogold (**E** and **E'**, red arrowheads) and then obtaining 3D reconstructions along that axon. **E** shows an early section in the series, and 3D reconstruction (**E'**) of the labeled axon (green) illustrates the ease of identifying the stimulated axons without obscuring the subcellular content of synaptic vesicles (magenta spheres), mitochondria (purple), and synapses (red) associated with postsynaptic dendritic spines. Labeling of a section near the end of the series (**E''**) ensures that the activated axon was followed. Adapted from Kuwajima et al. (2019).

ferentially after LTP in the adult and developing hippocampus remains an open and important question.

I actually began this journey studying dendritic spines of cerebellar Purkinje neurons (Fig. 13A, B; Harris and Stevens, 1988). The spines that synapse with the parallel fibers are sufficiently

uniform in shape that I felt confident in my budding ability to recognize and reconstruct them through serial EM sections. Several principles emerged. Most of the spines on a 5–10 μm dendritic segment made synapses with different presynaptic axons (Fig. 13C). When neighboring spines shared the same presynap-

tic axon, they were more uniform in size than spines that did not share the same presynaptic axons, and thus were less likely to have had the same activation history. When spines branched, different heads of the same branched spine did not share the same presynaptic axon; thus, like in hippocampus, cerebellar dendritic spines do not split (Fig. 13E). Interestingly, a parallel fiber that synapses with the nonspiny dendrite of an interneuron can also synapse with spines of a Purkinje cell dendrite.

Upon repeated stimulation, climbing fibers show paired-pulse depression (Fig. 13F), whereas the same stimulation delivered to parallel fibers results in paired-pulse facilitation (Fig. 13G). Our collaborators asked whether the frequency of docked synaptic vesicles at active zones could explain these profound differences in synapse function at climbing-fiber versus parallel-fiber synapses (Xu-Friedman et al., 2001). The outcomes showed that the number of docked vesicles at the release sites of climbing-fiber (Fig. 13H) and parallel-fiber synapses (Fig. 13I) did not differ significantly (Fig. 13J). Among other explanations, this outcome suggested that some docked vesicles are not release ready, an interpretation that is consistent with numerous molecular studies of synaptic vesicles.

A side trip into hippocampal area CA3 provided new knowledge about large spines called thorny excrescences (Chicurel and Harris, 1992). These spines emerge from the proximal dendrites to synapse with presynaptic boutons of the mossy fibers that arrive from dentate granule cells (Fig. 13K). Upon reconstruction, the spines were found to have multiple branches (Fig. 13L) that can synapse with one or more presynaptic boutons. Individual heads of these branches host a variety of subcellular structures: most have a postsynaptic density and contain smooth endoplasmic reticulum, about half contain polyribosomes, a third contain a multivesicular body, about a quarter have a spinule, and ~10% contain a mitochondrion and/or a microtubule (Fig. 13M). Although not yet quantified, it is obvious that many of the spine heads also contain other endocytic components such as vesicles and tubules in addition to the multivesicular bodies. The spine apparatus, which functions similarly to the Golgi apparatus, is also evident in some spine heads (Fig. 13N). Thus, these spines have virtually all of the subcellular components of the dendritic shaft, but these components are isolated locally in the vicinity of their synapses. The presynaptic mossy-fiber boutons contain giant clear vesicles nearly twice the size of the standard glutamatergic vesicles (Fig. 13N,O). These giant vesicles provide an anatomical correlate for the giant miniature EPSPs measured at these synapses (Fig. 13O, inset, arrow; Henze et al., 2002).

A brief encounter with the ant brain revealed large presynaptic boutons that synapse with multiple postsynaptic protrusions (Seid et al., 2005), similar to the mossy fiber boutons. Unlike synapses in the mammalian hippocampus, cortex, and cerebellum, however, each protrusion shared with other protrusions a continuous density that fills the extracellular space (Fig. 13P,Q). These shared densities occupy a greater area of the bouton in young ants than in old ants from the same colony (Fig. 13R,S).

Long ago, we noticed that spines from a single CA1 dendrite sharing inputs with the same presynaptic axon were more similar in size than spines arising from different dendrites, even if those spines shared the same presynaptic input (Fig. 14A; Sorra and Harris, 1993). Recent reconstructions showed that the heads of axon-coupled same-dendrite spines in both CA1 and dentate gyrus were well correlated with a very small variance in their dimensions (i.e., they were highly precise), whereas spine neck dimensions were not (Fig. 14B,C; Bartol et al., 2015; Bromer et

al., 2018). Consistent with many of our prior reports, these reconstructions showed good correlations among spine head volumes, PSD surface areas, and the number of docked and nondocked presynaptic vesicles (Harris and Stevens, 1988, 1989; Lisman and Harris, 1993; Harris and Kater, 1994; Sorra and Harris, 2000; Bartol et al., 2015; Bromer et al., 2018). Thus, we had a strong natural experiment for the application of signal detection theory to calculate information content in synapse size and plasticity.

Using signal detection theory, we compared spines *in vivo* in perfusion-fixed CA1, in dentate gyrus under control conditions, and in dentate synapses that had undergone induction of LTP at medial perforant path synapses (Bromer et al., 2018). LTP markedly increased the frequency of both small and large spines relative to control. This bidirectional expansion resulted in heterosynaptic counterbalancing of total synaptic area per unit length of granule cell dendrite, as in adult area CA1 (Fig. 5, above). Control hemispheres exhibited 6.5 distinct spine sizes for 2.7 bits of storage capacity, while LTP resulted in 12.9 distinct spine sizes (3.7 bits of storage capacity). In contrast, control hippocampal CA1 synapses exhibited 26 distinguishable synaptic sizes (4.7 bits of storage capacity) with much greater synaptic precision than either control or potentiated dentate gyrus synapses (Fig. 14D). Because of stochastic variability of synaptic activation, this precision requires averaging activity over several minutes. In the past, theorists have treated synapses as 1 bit computational machines, being on or off, excitatory or inhibitory. These findings show that baseline capacity is much greater, and that synaptic plasticity alters total capacity. Furthermore, hippocampal subregions differ dramatically in their synaptic information storage capacity, reflecting their diverse functions and activation histories.

Since the beginning, I have longed for a means to identify activated synapses at the ultrastructural level. In the past, we have interpreted outcomes by comparing populations of synapses with different activation histories, but the question always remained regarding exactly which synapses had been activated. For the LTP studies, the samples were near large concentric bipolar electrodes, so it is reasonable to assume that most of the synapses were activated differentially by the control and experimental stimulation paradigms. We have recently developed a new approach that should allow us to extend these findings along identified axons (Fig. 14E). We developed a recombinant adenovirus construct that expresses channelrhodopsin2 and mAPEX2 (Kuwajima et al., 2019). We proved that high-frequency optical activation specific to the labeled axons produces late-phase LTP. In slices fixed with our standard protocol, tyramide signal amplification catalyzed by mAPEX2 deposited Alexa Fluor dye in the targeted axons. The dye-containing axons were identified after embedding by immunogold labeling in a subset of thin sections in 3DEM series. In tSEM images of an axon containing immunogold labeling, we could easily identify the stimulated axons and their subcellular contents, including synaptic vesicles, mitochondria, and synapses associated with postsynaptic dendritic spines (Fig. 14E'). With this approach, we can discover whether the patterns of synaptic plasticity revealed through differential population analyses are specific to the activated spines.

We continue to work with our collaborators to explore the precision and variance of synapses across brain regions, various species, and ultimately in humans to understand the impact of brain disease on information storage. Please join us as we share the ongoing odyssey at SynapseWeb and 3DEM.org.

References

Bartol TM, Bromer C, Kinney J, Chirillo MA, Bourne JN, Harris KM, Sejnowski TJ (2015) Nanoconnectomic upper bound on the variability of synaptic plasticity. *Elife* 4:e10778.

Bell ME, Bourne JN, Chirillo MA, Mendenhall JM, Kuwajima M, Harris KM (2014) Dynamics of nascent and active zone ultrastructure as synapses enlarge during long-term potentiation in mature hippocampus. *J Comp Neurol* 522:3861–3884.

Bourne JN, Harris KM (2011) Coordination of size and number of excitatory and inhibitory synapses results in a balanced structural plasticity along mature hippocampal CA1 dendrites during LTP. *Hippocampus* 21:354–373.

Bourne JN, Kirov SA, Sorra KE, Harris KM (2007a) Warmer preparation of hippocampal slices prevents synapse proliferation that might obscure LTP-related structural plasticity. *Neuropharmacology* 52:55–59.

Bourne JN, Sorra KE, Hurlburt J, Harris KM (2007b) Polyribosomes are increased in spines of CA1 dendrites 2 h after the induction of LTP in mature rat hippocampal slices. *Hippocampus* 17:1–4.

Bourne JN, Chirillo MA, Harris KM (2013) Presynaptic ultrastructural plasticity along CA3—>CA1 axons during long-term potentiation in mature hippocampus. *J Comp Neurol* 521:3898–3912.

Bromer C, Bartol TM, Bowden JB, Hubbard DD, Hanka DC, Gonzalez PV, Kuwajima M, Mendenhall JM, Parker PH, Abraham WC, Sejnowski TJ, Harris KM (2018) Long-term potentiation expands information content of hippocampal dentate gyrus synapses. *Proc Natl Acad Sci USA* 115:E2410–E2418.

Cao G, Harris KM (2012) Developmental regulation of the late phase of long-term potentiation (L-LTP) and metaplasticity in hippocampal area CA1 of the rat. *J Neurophysiol* 107:902–912.

Cao G, Harris KM (2014) Augmenting saturated LTP by broadly spaced episodes of theta-burst stimulation in hippocampal area CA1 of adult rats and mice. *J Neurophysiol* 112:1916–1924.

Chicurel ME, Harris KM (1992) Three-dimensional analysis of the structure and composition of CA3 branched dendritic spines and their synaptic relationships with mossy fiber boutons in the rat hippocampus. *J Comp Neurol* 325:169–182.

Chirillo MA, Waters MS, Lindsey LF, Bourne JN, Harris KM (2019) Local resources of polyribosomes and SER promote synapse enlargement and spine clustering after long-term potentiation in adult rat hippocampus. *Sci Rep* 9:3861.

Cooney JR, Hurlburt JL, Selig DK, Harris KM, Fiala JC (2002) Endosomal compartments serve multiple hippocampal dendritic spines from a widespread rather than a local store of recycling membrane. *J Neurosci* 22: 2215–2224.

Cui-Wang T, Hanus C, Cui T, Helton T, Bourne J, Watson D, Harris KM, Ehlers MD (2012) Local zones of endoplasmic reticulum complexity confine cargo in neuronal dendrites. *Cell* 148:309–321.

Fiala JC, Harris KM (2001a) Cylindrical diameters method for calibrating section thickness in serial electron microscopy. *J Microsc* 202:468–472.

Fiala JC, Harris KM (2001b) Extending unbiased stereology of brain ultrastructure to three-dimensional volumes. *J Am Med Inform Assoc* 8:1–16.

Fiala JC, Harris KM (2002) Computer-based alignment and reconstruction of serial sections. *Microsc Anal (Am Ed)* 87:5–8.

Fiala JC, Feinberg M, Popov V, Harris KM (1998) Synaptogenesis via dendritic filopodia in developing hippocampal area CA1. *J Neurosci* 18: 8900–8911.

Fiala JC, Allwardt B, Harris KM (2002a) Dendritic spines do not split during hippocampal LTP or maturation. *Nat Neurosci* 5:297–298.

Fiala JC, Spacek J, Harris KM (2002b) Dendritic spine pathology: cause or consequence of neurological disorders? *Brain Res Brain Res Rev* 39: 29–54.

Fiala JC, Kirov SA, Feinberg MD, Petrak LJ, George P, Goddard CA, Harris KM (2003) Timing of neuronal and glial ultrastructure disruption during brain slice preparation and recovery in vitro. *J Comp Neurol* 465:90–103.

Harris KM (1999) Structure, development, and plasticity of dendritic spines. *Curr Opin Neurobiol* 9:343–348.

Harris KM, Kater SB (1994) Dendritic spines: cellular specializations imparting both stability and flexibility to synaptic function. *Annu Rev Neurosci* 17:341–371.

Harris KM, Landis DM (1986) Membrane structure at synaptic junctions in area CA1 of the rat hippocampus. *Neuroscience* 19:857–872.

Harris KM, Stevens JK (1988) Dendritic spines of rat cerebellar Purkinje cells: serial electron microscopy with reference to their biophysical characteristics. *J Neurosci* 8:4455–4469.

Harris KM, Stevens JK (1989) Dendritic spines of CA1 pyramidal cells in the rat hippocampus: serial electron microscopy with reference to their biophysical characteristics. *J Neurosci* 9:2982–2997.

Harris KM, Teylor TJ (1983) Evidence for late development of inhibition in area CA1 of the rat hippocampus. *Brain Res* 268:339–343.

Harris KM, Teylor TJ (1984) Developmental onset of long-term potentiation in area CA1 of the rat hippocampus. *J Physiol* 346:27–48.

Harris KM, Cruce WL, Greenough WT, Teylor TJ (1980) A golgi impregnation technique for thin brain slices maintained in vitro. *J Neurosci Methods* 2:363–371.

Harris KM, Jensen FE, Tsao B (1989) Ultrastructure, development, and plasticity of dendritic spine synapses in area CA1 of the rat hippocampus: extending our vision with serial electron microscopy and three-dimensional analyses. In: *The hippocampus: new vistas: neurology and neurobiology series, Vol 52* (Chan-Palay and Kohler, eds), pp 33–52. New York: Liss.

Harris KM, Jensen FE, Tsao B (1992) Three-dimensional structure of dendritic spines and synapses in rat hippocampus (CA1) at postnatal day 15 and adult ages: implications for the maturation of synaptic physiology and long-term potentiation. *J Neurosci* 12:2685–2705.

Harris KM, Perry E, Bourne J, Feinberg M, Ostroff L, Hurlburt J (2006) Uniform serial sectioning for transmission electron microscopy. *J Neurosci* 26:12101–12103.

Harris KM, Spacek J, Bell ME, Parker PH, Lindsey LF, Baden AD, Vogelstein JT, Burns R (2015) A resource from 3D electron microscopy of hippocampal neuropil for user training and tool development. *Sci Data* 2:150046.

Henze DA, McMahon DB, Harris KM, Barrionuevo G (2002) Giant miniature EPSCs at the hippocampal mossy fiber to CA3 pyramidal cell synapse are monoquantal. *J Neurophysiol* 87:15–29.

Jackson PS, Suppes T, Harris KM (1993) Stereotypical changes in the pattern and duration of long-term potentiation expressed at postnatal days 11 and 15 in the rat hippocampus. *J Neurophysiol* 70:1412–1419.

Jensen FE, Harris KM (1989) Preservation of neuronal ultrastructure in hippocampal slices using rapid microwave-enhanced fixation. *J Neurosci Methods* 29:217–230.

Kinney JP, Spacek J, Bartol TM, Bajaj CL, Harris KM, Sejnowski TJ (2013) Extracellular sheets and tunnels modulate glutamate diffusion in hippocampal neuropil. *J Comp Neurol* 521:448–464.

Kirk LM, Zatyko K, Bromer C, Bartol T, Sejnowski T, Harris KM (2018) Presynaptic ultrastructure changes in response to LTP stimulation in stratum radiatum of hippocampal CA1 neuropil. *Soc Neurosci Abstr* 40: 202.11.

Kirov SA, Harris KM (1999) Dendrites are more spiny on mature hippocampal neurons when synapses are inactivated. *Nat Neurosci* 2: 878–883.

Kirov SA, Sorra KE, Harris KM (1999) Slices have more synapses than perfusion-fixed hippocampus from both young and mature rats. *J Neurosci* 19:2876–2886.

Kirov SA, Goddard CA, Harris KM (2004a) Age-dependence in the homeostatic upregulation of hippocampal dendritic spine number during blocked synaptic transmission. *Neuropharmacology* 47:640–648.

Kirov SA, Petrak LJ, Fiala JC, Harris KM (2004b) Dendritic spines disappear with chilling but proliferate excessively upon rewarming of mature hippocampus. *Neuroscience* 127:69–80.

Kulik YD, Watson DJ, Cao G, Kuwajima M, Harris KM (2019) Structural plasticity of dendritic secretory compartments during LTP-induced synaptogenesis. *Elife* 8:e46356.

Kuwajima M, Mendenhall JM, Harris KM (2013a) Large-volume reconstruction of brain tissue from high-resolution serial section images acquired by SEM-based scanning transmission electron microscopy. *Methods Mol Biol* 950:253–273.

Kuwajima M, Spacek J, Harris KM (2013b) Beyond counts and shapes: studying pathology of dendritic spines in the context of the surrounding neuropil through serial section electron microscopy. *Neuroscience* 251: 75–89.

Kuwajima M, Mendenhall JM, Lindsey LF, Harris KM (2013c) Automated transmission-mode scanning electron microscopy (tSEM) for large volume analysis at nanoscale resolution. *PLoS One* 8:e59573.

Kuwajima M, Ostrovskaya OI, Cao G, Weisberg SA, Harris KM, Zemelman BV (2019) Ultrastructure of light-activated axons following optogenetic stimulation to produce late-phase long-term potentiation. *bioRxiv*. Advance online publication. Retrieved December 4, 2019. doi:10.1101/799890.

Lisman JE, Harris KM (1993) Quantal analysis and synaptic anatomy—integrating two views of hippocampal plasticity. *Trends Neurosci* 16:141–147.

Mishchenko Y, Hu T, Spacek J, Mendenhall J, Harris KM, Chklovskii DB (2010) Ultrastructural analysis of hippocampal neuropil from the connectomics perspective. *Neuron* 67:1009–1020.

Ostroff LE, Fiala JC, Allwardt B, Harris KM (2002) Polyribosomes redistribute from dendritic shafts into spines with enlarged synapses during LTP in developing rat hippocampal slices. *Neuron* 35:535–545.

Ostroff LE, Watson DJ, Cao G, Parker PH, Smith H, Harris KM (2018) Shifting patterns of polyribosome accumulation at synapses over the course of hippocampal long-term potentiation. *Hippocampus* 28:416–430.

Ostrovskaya OI, Cao G, Eroglu C, Harris KM (2019) Developmental onset of enduring long-term potentiation in mouse hippocampus. *BioRxiv*. Advanced online publication. Retrieved December 4, 2019. doi:10.1101/787192.

Ouyang Y, Kantor D, Harris KM, Schuman EM, Kennedy MB (1997) Visualization of the distribution of autophosphorylated calcium/calmodulin-dependent protein kinase II after tetanic stimulation in the CA1 area of the hippocampus. *J Neurosci* 17:5416–5427.

Park M, Salgado JM, Ostroff L, Helton TD, Robinson CG, Harris KM, Ehlers MD (2006) Plasticity-induced growth of dendritic spines by exocytic trafficking from recycling endosomes. *Neuron* 52:817–830.

Seid MA, Harris KM, Traniello JF (2005) Age-related changes in the number and structure of synapses in the lip region of the mushroom bodies in the ant *pheidole dentata*. *J Comp Neurol* 488:269–277.

Shepherd GM, Harris KM (1998) Three-dimensional structure and composition of CA3—>CA1 axons in rat hippocampal slices: implications for presynaptic connectivity and compartmentalization. *J Neurosci* 18:8300–8310.

Smith HL, Bourne JN, Cao G, Chirillo MA, Ostroff LE, Watson DJ, Harris KM (2016) Mitochondrial support of persistent presynaptic vesicle mobilization with age-dependent synaptic growth after LTP. *Elife* 5:e15275.

Sorra KE, Harris KM (1993) Occurrence and three-dimensional structure of multiple synapses between individual radiatum axons and their target pyramidal cells in hippocampal area CA1. *J Neurosci* 13:3736–3748.

Sorra KE, Harris KM (1998) Stability in synapse number and size at 2 hr after long-term potentiation in hippocampal area CA1. *J Neurosci* 18:658–671.

Sorra KE, Harris KM (2000) Overview on the structure, composition, function, development, and plasticity of hippocampal dendritic spines. *Hippocampus* 10:501–511.

Sorra KE, Fiala JC, Harris KM (1998) Critical assessment of the involvement of perforations, spinules, and spine branching in hippocampal synapse formation. *J Comp Neurol* 398:225–240.

Sorra KE, Mishra A, Kirov SA, Harris KM (2006) Dense core vesicles resemble active-zone transport vesicles and are diminished following synaptogenesis in mature hippocampal slices. *Neuroscience* 141:2097–2106.

Spacek J, Harris KM (1997) Three-dimensional organization of smooth endoplasmic reticulum in hippocampal CA1 dendrites and dendritic spines of the immature and mature rat. *J Neurosci* 17:190–203.

Spacek J, Harris KM (1998) Three-dimensional organization of cell adhesion junctions at synapses and dendritic spines in area CA1 of the rat hippocampus. *J Comp Neurol* 393:58–68.

Spacek J, Harris KM (2004) Trans-endocytosis via spinules in adult rat hippocampus. *J Neurosci* 24:4233–4241.

Teyler TJ, Perkins AT 4th, Harris KM (1989) The development of long-term potentiation in hippocampus and neocortex. *Neuropsychologia* 27:31–39.

Ventura R, Harris KM (1999) Three-dimensional relationships between hippocampal synapses and astrocytes. *J Neurosci* 19:6897–6906.

Watson DJ, Ostroff L, Cao G, Parker PH, Smith H, Harris KM (2016) LTP enhances synaptogenesis in the developing hippocampus. *Hippocampus* 26:560–576.

Witcher MR, Kirov SA, Harris KM (2007) Plasticity of perisynaptic astroglia during synaptogenesis in the mature rat hippocampus. *Glia* 55:13–23.

Witcher MR, Park YD, Lee MR, Sharma S, Harris KM, Kirov SA (2010) Three-dimensional relationships between perisynaptic astroglia and human hippocampal synapses. *Glia* 58:572–587.

Xu-Friedman MA, Harris KM, Regehr WG (2001) Three-dimensional comparison of ultrastructural characteristics at depressing and facilitating synapses onto cerebellar Purkinje cells. *J Neurosci* 21:6666–6672.